Journal of Instrumentation

OPEN ACCESS

First beam tests of prototype silicon modules for the CMS High Granularity Endcap Calorimeter

To cite this article: N. Akchurin *et al* 2018 *JINST* **13** P10023

View the article online for updates and enhancements.

IOP ebooks™

Bringing you innovative digital publishing with leading voices to create your essential collection of books in STEM research.

Start exploring the collection - download the first chapter of every title for free.

This content was downloaded from IP address 188.184.3.52 on 25/10/2018 at 11:45

Published by IOP Publishing for Sissa Medialab

Received: *April 19, 2018*
Revised: *August 23, 2018*
Accepted: *September 20, 2018*
Published: *October 18, 2018*

First beam tests of prototype silicon modules for the CMS High Granularity Endcap Calorimeter

N. Akchurin,[r] A. Apreysan,[o] S. Banerjee,[o] D. Barney,[g,1] B. Bilki,[t] A. Bornheim,[m] J. Bueghly,[q] S. Callier,[c] V. Candelise,[h] Y.-H. Chang,[h] Y.-W. Chang,[h] R. Chatterjee,[u] K-Y. Cheng,[h] C-H. Chien,[i] E. Curras Rivera,[v] C. de la Taille,[c] J. Eckdahl,[s] E. Frahm,[u] N. Frank,[g] J. Freeman,[o] D. Gawerc,[m] Z. Gecse,[o] C. Ginghu,[o] H. Gonzalez,[o] T. Hawke,[o] J. Incandela,[s] S. Jain,[e] S. Jain,[h] H.-R. Jheng,[h] M. Jonas,[o] O. Kara,[j] R. Khurana,[h] G. Kopp,[m] A. Kumar,[q] S. Kunori,[r] C.-M. Kuo,[h] S. Kyre,[s] D. Lazic,[l] B. Li,[a] H. Liao,[a] R. Lipton,[o] L. Linssen,[g] A. Lobanov,[b] R.-S. Lu,[i] A. Maier,[g] G. Majumder,[e] M. Mannelli,[g] A. Martelli,[g] L. Mastrolorenzo,[k] T. Mengke,[r] M. Miller,[s] M. Moll,[g] J. Morant,[g] T. Mudholkar,[n] N. Odell,[q] E. Paganis,[i] M. Paulini,[n] C. Pena,[m] P. Petiot,[g] L. Pezzotti,[f] F. Pitters,[g] A. Pozdnyakov,[h] H. Prosper,[p] A. Psallidas,[i] T. Quast,[g] R. Quinn,[u] F. Romeo,[a] A. Roy,[d] P. Rubinov,[o] R. Rusack,[u] E. Sicking,[g] A. Steen,[i] M. Sun,[n] I. Tarasov,[g] D. Thienpont,[c] E. Tiras,[t] T. Virdee,[k] F. Wang,[a] M. Weinberg,[n] D. White,[s] S. Xie,[m] S.-S. Yu,[h] H. Zhang[a] and Z. Zhang[m]

[a] *Insitute for High Energy Physics, Beijing, China*
[b] *Laboratoire Leprince-Ringuet, Palaiseau, France*
[c] *Organization for Microelectronics design and Applications (OMEGA), Palaiseau, France*
[d] *Saha Institute of Nuclear Physics, Kolkata, India*
[e] *Tata Institute for Fundamental Research, Bombay, India*
[f] *University of Pavia, Pavia, Italy*
[g] *CERN, Geneva, Switzerland*
[h] *National Central University, Chung-Li, Taiwan*
[i] *National Taiwan University, Taipei, Taiwan*
[j] *Cukurova University, Adana, Turkey*
[k] *Imperial College of Science, Technology and Medicine, London, U.K.*
[l] *Boston University, Boston, U.S.A.*
[m] *California Insitute of Technology, Pasadena, U.S.A.*
[n] *Carnegie Mellon University, Pittsburg, U.S.A.*
[o] *Fermi National Accelerator Laboratory, Batavia, U.S.A.*
[p] *Florida State University, Tallahassee, U.S.A.*
[q] *Northwestern University, Evanston, U.S.A.*

[1] Corresponding author.

© 2018 CERN for the benefit of the CMS collaboration. Published by IOP Publishing Ltd on behalf of Sissa Medialab. Original content from this work may be used under the terms of the Creative Commons Attribution 3.0 licence. Any further distribution of this work must maintain attribution to the author(s) and the title of the work, journal citation and DOI.

https://doi.org/10.1088/1748-0221/13/10/P10023

2018 JINST 13 P10023

[r] *Texas Tech. University, Lubbock, U.S.A.*
[s] *University of California Santa Barbara, Santa Barbara, U.S.A.*
[t] *University of Iowa, Iowa, U.S.A.*
[u] *University of Minnesota, Minneapolis, U.S.A.*
[v] *CERN, Geneva, Switzerland and Universidad de Cantabria, Cantabria, Spain*

E-mail: David.Barney@cern.ch

Abstract: The High Luminosity phase of the Large Hadron Collider will deliver 10 times more integrated luminosity than the existing collider, posing significant challenges for radiation tolerance and event pileup on detectors, especially for forward calorimetry. As part of its upgrade program, the Compact Muon Solenoid collaboration is designing a high-granularity calorimeter (HGCAL) to replace the existing endcap calorimeters. It will feature unprecedented transverse and longitudinal readout and triggering segmentation for both electromagnetic and hadronic sections. The electromagnetic section and a large fraction of the hadronic section will be based on hexagonal silicon sensors of 0.5–1 cm^2 cell size, with the remainder of the hadronic section being based on highly-segmented scintillators with silicon photomultiplier readout. The intrinsic high-precision timing capabilities of the silicon sensors will add an extra dimension to event reconstruction, especially in terms of pileup rejection. First hexagonal silicon modules, using the existing Skiroc2 front-end ASIC developed for CALICE, have been tested in beams at Fermilab and CERN in 2016. We present results from these tests, in terms of system stability, calibration with minimum-ionizing particles and resolution (energy, position and timing) for electrons, and the comparisons of these quantities with GEANT4-based simulation.

Keywords: Calorimeters; Performance of High Energy Physics Detectors; Si microstrip and pad detectors; Large detector systems for particle and astroparticle physics

2018 JINST 13 P10023

Contents

1 Overview of HGCAL and goals of the 2016 beam-test campaign **2**

2 Module construction, support structures and readout summary **3**
2.1 Silicon sensors 4
2.1.1 Characterization of the silicon sensors 5
2.2 Front-end electronics 6
2.3 DAQ chain 6
2.4 Mechanics & powering 8

3 Beam test setup, data summary, simulation and analysis framework **9**
3.1 Experimental configurations 9
3.2 Data taken 11
3.3 Triggering and particle selection 11
3.4 Simulation framework 11
3.4.1 Silicon energy deposits: data vs. simulation 12
3.5 The data analysis framework, data preparation and reconstruction 12

4 Stability and calibration **14**
4.1 Pedestal and noise: values and stability 14
4.2 Calibration with single particles 16
4.3 Gain calibration 18

5 Measurements of shower shapes, energy and position **19**
5.1 Longitudinal and transverse shower shapes 19
5.1.1 Longitudinal shower shapes 20
5.1.2 Transverse shower profiles 22
5.2 Energy measurements and resolution 23
5.3 Position resolution 27
5.3.1 Reference measurement 28
5.3.2 Position reconstruction 28

6 Precision timing with silicon diodes and modules **30**
6.1 Precision timing with silicon diodes 30
6.2 Precision timing with modules 34

7 Summary **37**

2018 JINST 13 P10023

1 Overview of HGCAL and goals of the 2016 beam-test campaign

The present CMS electromagnetic and hadronic endcap calorimeters will suffer irrecoverable radiation damage by the end of LHC running in 2023. To sustain the much higher radiation and to mitigate the extreme pile-up environment during operation at the High Luminosity-LHC (HL-LHC, 2025 onwards), the CMS collaboration has decided to replace its current endcap calorimeters with a new high-granularity endcap calorimeter known as "HGCAL" [1]. The HGCAL is a sampling calorimeter with silicon and plastic scintillator active materials. It includes both electromagnetic (CE-E) and hadronic (CE-H) sections. The former will use lead as the main absorber material and hexagonal silicon sensors as the active detector. It should be noted that the original engineering design of the CE-E, as described in the HGCAL Technical Proposal [2], used tungsten absorbers and not lead. For the tests presented in this paper we thus used tungsten as the main absorber.

The CE-H will use stainless steel as the absorber and a mixture of silicon (in the regions of highest radiation) and scintillator as detectors. An overview of the HGCAL design is shown in figure 1.

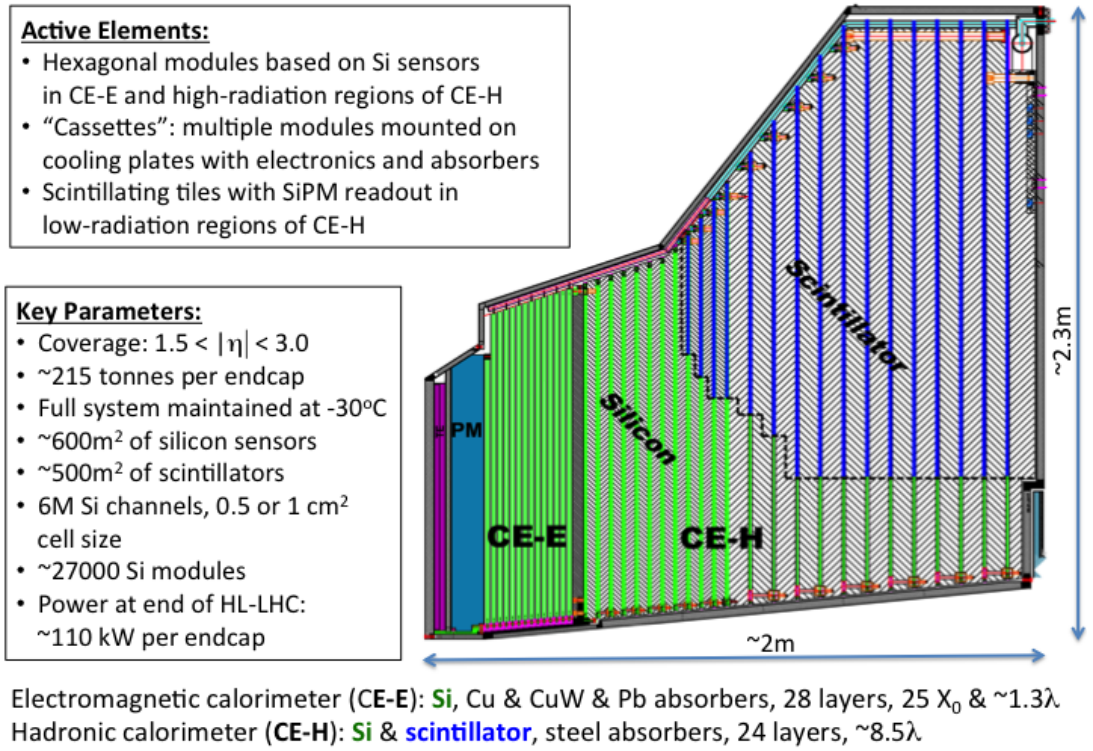

Figure 1. Overview of the basic design and coverage of the CMS high-granularity endcap calorimeter (HGCAL)

An extensive prototyping phase of HGCAL began in 2015. Hexagonal silicon sensors were procured and procedures developed to assemble modules using pre-existing front-end ASICs: the Skiroc2 [3] chip developed by the CALICE collaboration. The modules were rather novel, featuring deep-wire-bonding through holes in the printed circuit board (PCB) to the silicon sensor glued beneath. In order to validate the design of these modules, and of the HGCAL electromagnetic

2018 JINST 13 P10023

section in general, beam-tests at FNAL (Fermilab Testbeam Facility [4]) and CERN (SPS H2 beamline [5]) were carried-out, using custom DAQ boards based on off-the-shelf components. In addition to validating the HGCAL design, the main goals of the beam tests were to measure the performance and compare with a detailed simulation.

The construction of the modules is described in section 2. A summary of the setups and data taken at both FNAL and CERN, as well as the simulation and analysis frameworks, is presented in section 3, including specifics of the beam-lines used. Section 4 presents the stability of the systems and the calibration procedures and results. The measurements of shower shapes, energy and position are given in section 5, whilst section 6 summarises measurements of the timing performance of dedicated setups. Section 7 provides a summary and outlook.

2 Module construction, support structures and readout summary

The HGCAL silicon modules were hexagonal assemblies comprising a baseplate, a polyimide foil, a silicon sensor and a PCB, as shown schematically in figure 2.

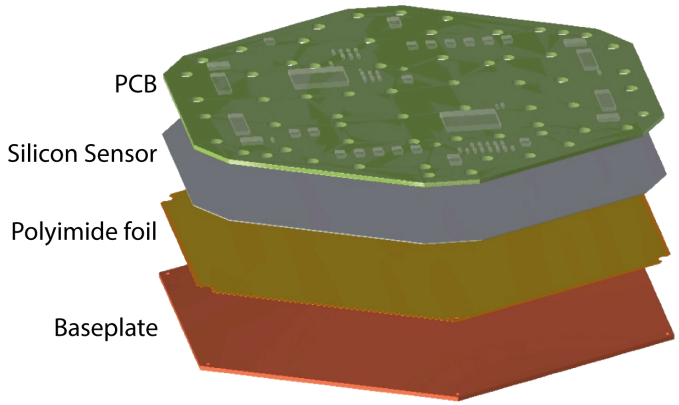

Figure 2. HGCAL silicon module schematic, showing the stacked layers.

The 2016 testbeam modules followed closely this design. Each module consisted of a copper-tungsten (25% Cu:75% W) hexagonal baseplate, a polyimide gold-surfaced sheet to allow biasing of the back side of the silicon sensor, the sensor itself, and a pair of PCBs for the front-end electronics. This latter differs from the final HGCAL design, which only has a single PCB for the front-end electronics. The function of the CuW plate was threefold: it provided mechanical rigidity to the module; it supplied a thermal pathway from the heat load of the ASICs on the PCB, through the silicon to the copper cooling plate supporting the module; and it was part of the calorimeter absorber. The CuW has a coefficient of thermal expansion close to that of silicon. The baseplates were made in three thicknesses: 0.8 mm ($\sim 0.15\ X_0$), 1.2 mm ($\sim 0.25\ X_0$) and 1.6 mm ($\sim 0.5\ X_0$). The first PCB in the pair connected electrically to the front side of the silicon cells with aluminium wire bonds through holes in the PCB and routed these signals to two small connectors. The second "readout PCB", which connected to the first, contained the front-end electronics and connectors to the outside world. This double-PCB design was chosen for flexibility, so that the readout PCB could be changed if any active element failed.

2018 JINST 13 P10023

The baseplate, polyimide sheet, silicon and first PCB were all glued together using Araldite 2011 non-conductive epoxy. This assembly was performed using a semi-automated gantry system for holding the pieces and dispensing optimized patterns of glue. The glue cured at room temperature in 24 hours, leading to a total assembly time of approximately three days for the three gluing steps. Three modules could be constructed in parallel. The assembly process is summarized in figure 3 and figure 4. The silicon pads were then connected to the signal lines on the PCB using aluminium wire bonds, which required a deep-access wire-bonding machine for the through-holes. Wire bonds also connected the PCB to the gold top surface of the polyimide sheet, which was glued (using conductive epoxy) to the backside of the silicon. The final step was to plug the readout PCB onto the first and test the module.

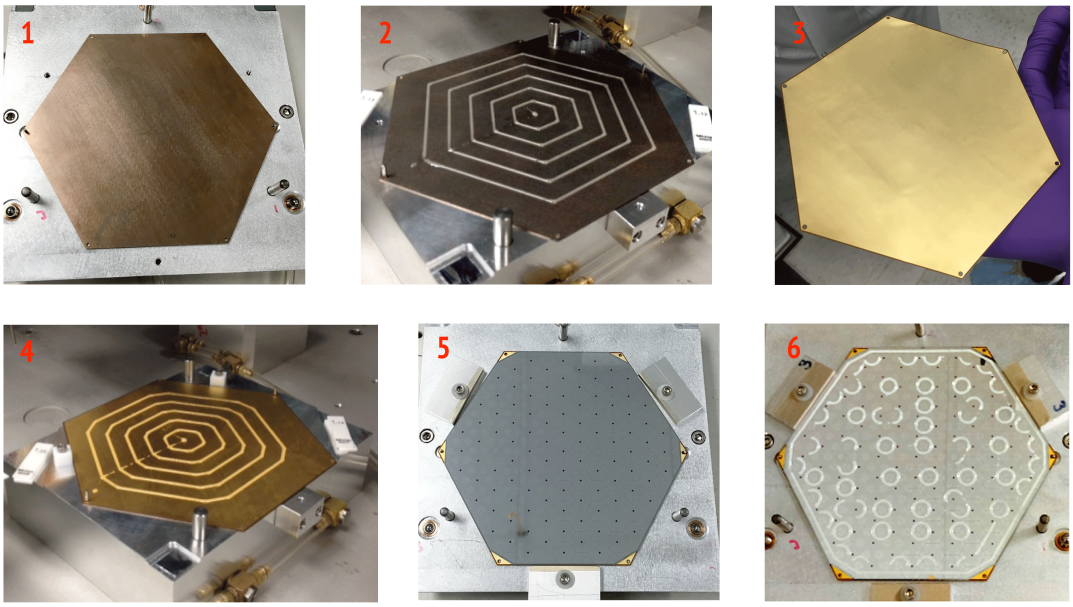

Figure 3. The assembly of one of the modules used in the 2016 beam tests, until the PCB-mounting stage. 1: the CuW baseplate on its gluing jig; 2: addition of Araldite 2011 epoxy; 3: the polyimide gold-plated foil; 4: the polyimide foil glued to the baseplate and with its own layer of glue; 5: the silicon sensor glued onto the polyimide foil; 6: the addition of a special pattern of glue that, when the PCB was attached, spread over the entire silicon surface except where the wire-bonding took place.

2.1 Silicon sensors

The physical thickness of the silicon sensors was 320 µm with a depleted (active) thickness of 200 µm. The majority of the cells on the sensor were hexagonal with an area of ~ 1.1 cm^2. There were two hexagonal cells divided into two parts: an inner "calibration pad", having an area of about 1/9th of the area of the full hexagonal cell, and the surrounding "outer calibration cell". The former facilitate calibration with single mimimum-ionizing particles (MIPs) (see section 4.2) after irradiation, when the S/N of a standard cell may be too small to detect single MIPs efficiently: the smaller area results in a smaller capacitance, which then decreases the intrinsic noise of the cell, whilst the MIP signal size stays the same. The sensors have half-hexagonal cells at the edges and so-called "mousebite cells" at the corners. There were 134 individual cells on each sensor.

2018 JINST 13 P10023

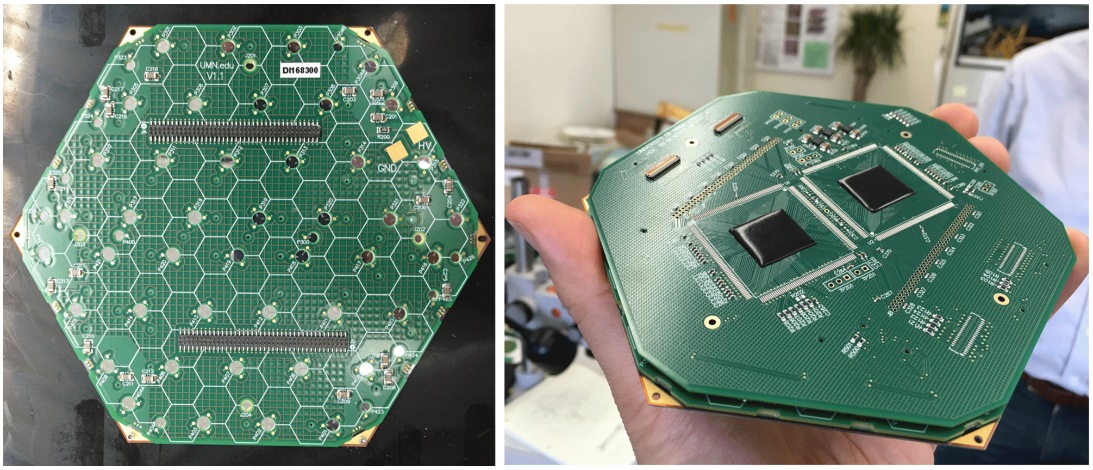

Figure 4. Left: photo of the bare module showing the PCB with connectors and holes for wire bonds. The polyimide layer is visible at the corners, as well as holes through the baseplate for attaching it to a support (cooling) plate. Right: complete 2016 module showing the readout PCB with two wire-bonded Skiroc2 bare-die ASICs (under protective black potting material)

As this exceeds the number of electronic channels available in the pair of front-end ASICs (128), some pairs of cells at the sensor periphery were electrically connected on the PCB to form "merged mousebites" and "merged cells", resulting in a total of 127 readout channels. This left one channel unconnected, which could be used for charge injection purposes. Figure 5 shows one of the 6″ p-in-n hexagonal silicon sensor, manufactured by HPK.[1] The different types of cell and readout channel are shown.

The numbers of each type of cell and readout channel are summarised in table 1.

Table 1. The numbers and types of sensor cells and readout channels for a single silicon sensor from the 2016 beam tests.

	Sensor cells	Readout channels
Full hexagons	106	103
Half hexagons	12	12
Mousebite cells	12	0
Inner calibration cells	2	2
Outer calibration cells	2	2
Merged mousebites	0	4
Merged cells	0	4
Total	134	127

2.1.1 Characterization of the silicon sensors

Thirty silicon sensors were characterized at FNAL using a custom-built probe card featuring light-touch "pogo pins" for electronic connection. Standard switching units and power/measurement devices were used, to measure the IV characteristics (including breakdown voltage) and CV curves (to determine full-depletion voltage).

[1]Hamamatsu Photonics, Hamamatsu, Japan.

2018 JINST 13 P10023

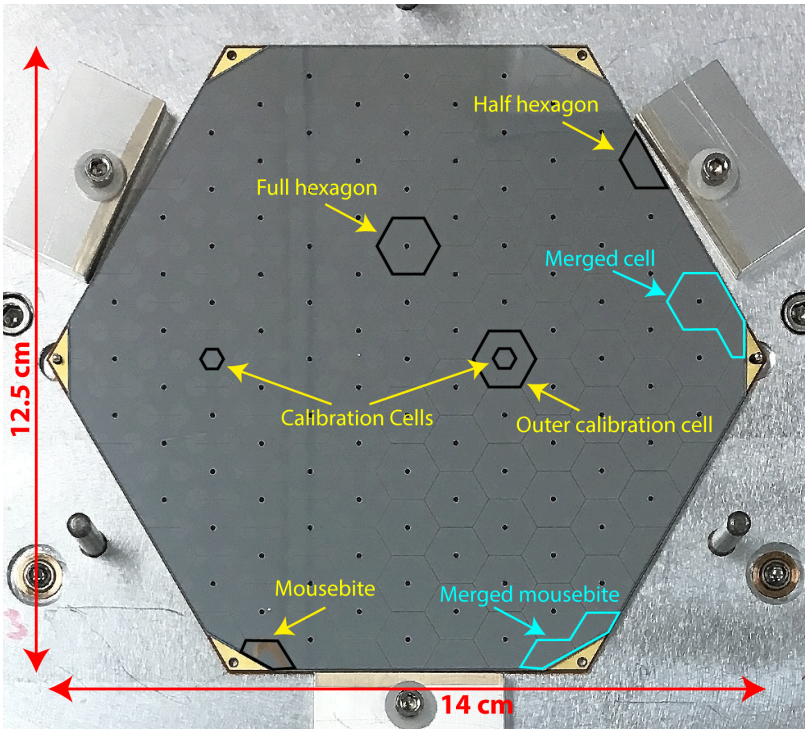

Figure 5. A hexagonal silicon sensor used in the beam tests, showing the cell types as well as the merged cells (done at the level of the PCB).

The sensors showed excellent performance, all reaching 1000 V (the specification for the HGCAL) without breaking-down. Depletion was around 120 V and, at this voltage, the average leakage current for the whole sensor was less than 50 nA, corresponding to an average leakage current per cell of less than 0.1 nA, increasing by about a factor 3 at 1000 V. Figure 6 shows the leakage current per cell (in nA) in a typical 200 µm-thick sensor, at both 120 V and 1000 V.

2.2 Front-end electronics

For these first proof-of-principle beam tests, an existing ASIC was used: "Skiroc2" [3]. Skiroc2 was developed for the CALICE [6] collaboration with silicon-based calorimetry in mind. The chip offers a rich functionality of which only a fraction was used. Each Skiroc2 has 64 channels, with each channel having a preamplifier and two separate slow shapers, a fast shaper, self-trigger and fifteen-cell pipeline, as well as a 12-bit ADC. Only the slow shapers were used in our system as we utilized an external trigger (the fast shaper could be used for self-trigger). The two shapers have a fixed gain ratio of 1:10, providing low- and high-gain amplification and hence a large dynamic range with, at the same time, good accuracy for small signals from single particles. A simplified schematic of the Skiroc2 ASIC is shown in figure 7.

2.3 DAQ chain

Two Skiroc2 ASICs were mounted on each readout PCB. The board layout was such that it could accomodate either bare die or quad-flat-pack (QFP) packaged chips. The compact nature of the CE requires low-profile connectivity to minimize the space between consecutive absorbers/cassettes. This

2018 JINST 13 P10023

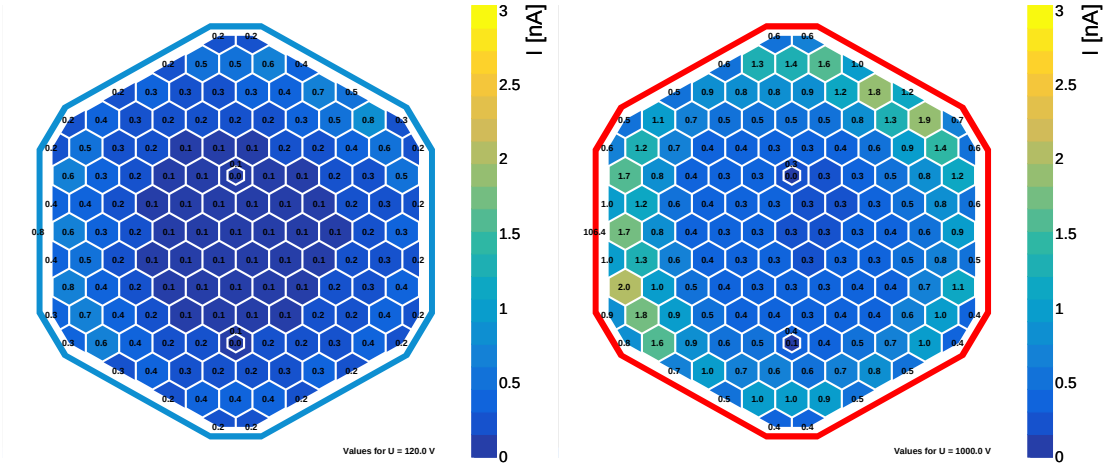

Figure 6. The current per cell for a typical hexagonal silicon sensor used in the 2016 beam tests, prior to it being assembled into a module, at 120 V (left) and 1000 V (right). The border surrounding the sensor represents the leakage current measured in the guard ring at the edge of the sensor.

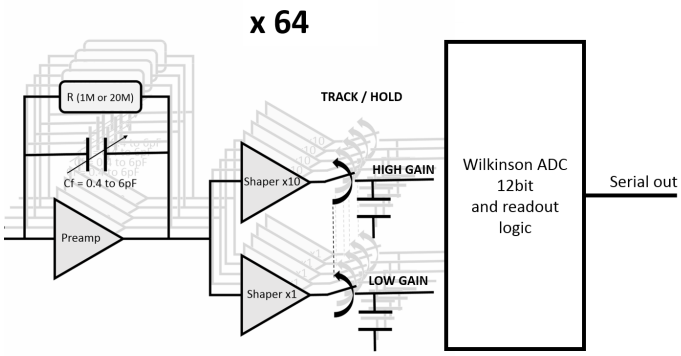

Figure 7. A simplified schematic of the Skiroc2 ASIC, showing only the sections used in the 2016 beam tests.

was achieved with commercially-available flexible polyimide cables and corresponding surface-mount connectors. The digital data from the Skiroc2s were carried by two flexible cables to a passive right-angle adapter PCB, then through another pair of flexible cables to 6U "DDC" — Dual-Daughterboard Carrier cards. These DDC hosted two "FMCIO" mezzanines, utilizing standard FMC (FPGA Mezzanine Card) connectors and incorporating Xilinx XC7A100T "Artix" FPGAs. The DDC routed the signals from two FMCIO (hence two modules) to a standard HDMI connector. Another commercially-available board, the "Zedboard" [7], was used to accumulate data from up to 14 DDCs through another passive custom board, known as the "ZEDIO". All trigger and control signals were routed from the Zedboard through the other boards mentioned above to the Skiroc2s. A single Zedboard was therefore capable of controlling and reading data from up to 28 modules, corresponding to one module per layer in a complete 28-layer CE-E prototype, with 3564 electronic channels. The final link was from the Zedboard to a standard PC through ethernet. A photograph of the full DAQ chain [8] is shown in figure 8.

2018 JINST 13 P10023

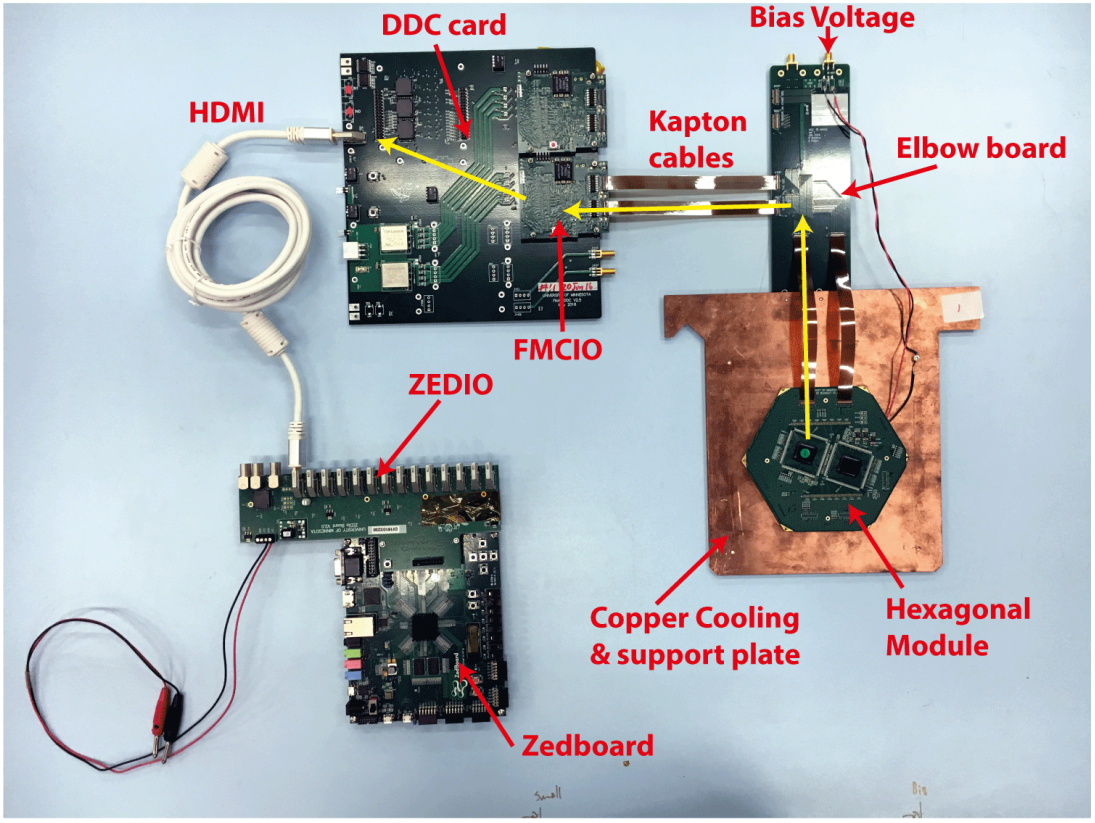

Figure 8. The complete DAQ system from module to Zedboard. The yellow arrows represent the data path from the module.

2.4 Mechanics & powering

The modules were attached to 6 mm (0.4 X_0) thick copper plates, as shown in figure 8. These plates had embedded channels to allow the flow of a cooling fluid, although this feature was not used in 2016. One module could be placed on either side of the copper plate. This was similar to the final HGCAL design, where groups of between about 25 and 100 modules will be mounted on wedge-shaped cooling plates to form "cassettes".[2]

A flexible mechanical support system was built, utilizing a "hanging file" design (see figure 9) for easy insertion of modules (attached to cooling plates) and absorber plates, which allowed different configurations to be explored. Aluminium frames supporting tungsten plates of three different thicknesses (2 mm: $\sim$ 0.57 X_0; 2.8 mm: $\sim$ 0.87 X_0; 4 mm: $\sim$ 1.14 X_0) were used as absorbers. The HGCAL prototype was designed such that the thickness of tungsten absorber (between two silicon sensors on two consecutive cassettes) was approximately equal to the amount of material (CuW + Cu + CuW) between two silicon sensors on a double-sided cassette. The frame also supported a 6U Eurochassis card cage housing the DDC cards.

[2]In the CE-E the cassettes will have silicon modules on both sides of the cooling plate, cover an angle of 60 degrees and will be self-supporting, containing lead absorbers on either side. In CE-H the cassettes will be single-sided, cover an angle of 30 degrees and will slide in between steel absorbers. The downstream layers of CE-H will also be mixtures of silicon modules and scintillator/SiPM modules — see [1] for more details.

2018 JINST 13 P10023

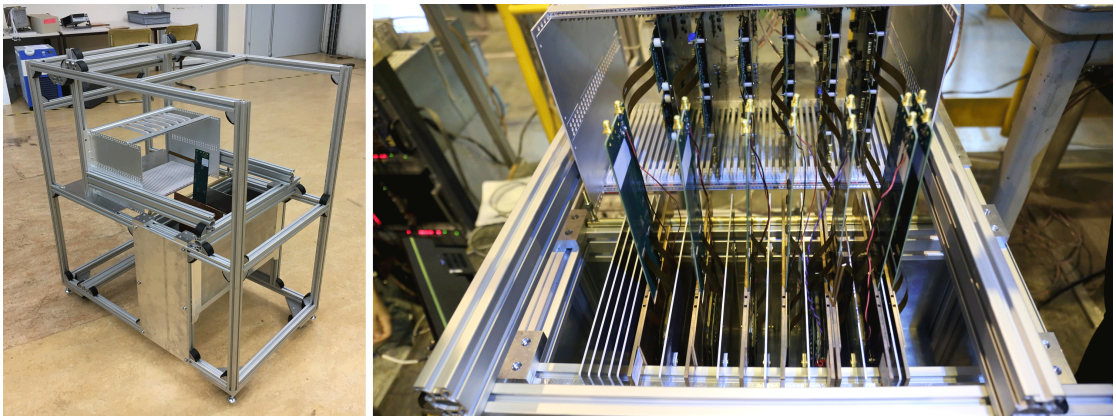

Figure 9. The hanging-file mechanics used to support the modules and absorbers. The right-hand image is a closeup of the structure when some modules and absorbers had been inserted. The DDC cards in the 6U crate are also visible.

A Delta Elektronika power supply provided, through a distribution board, 12V DC to the DDCs. Voltage regulators on these cards then supplied a stable 3.3V down to the Skiroc2 ASICs through the polyimide cables. A CAEN SY1527 mainframe equipped with a CAEN A1511B floating 0-500 V high-voltage module provided, again through a distribution board, the bias voltage for the silicon sensors through SMA cables to the "elbow" boards. Wires from these boards were soldered to the modules. Decoupling capacitors were on both the elbow board and modules.

3 Beam test setup, data summary, simulation and analysis framework

3.1 Experimental configurations

Three different configurations of absorbers and active layers were used at FNAL and CERN, exploiting the flexible mechanics.

At FNAL, sixteen modules were available, arranged as eight double-sided layers interspersed with tungsten absorbers. The total thickness of the setup at FNAL was deliberately limited to about 15 X_0 due to the relatively low energy electron beams available at FNAL (max. 32 GeV). Figure 10 shows a schematic of the FNAL setup.

At CERN, only eight modules were available but two configurations were explored. The first focused on the electromagnetic shower maximum for high-energy electrons, having the modules placed between about 6 X_0 and 15 X_0. The second setup had modules covering a more extensive longitudinal region, from 5 X_0 to 27 X_0. This latter also included some lead layers, in order to reach the required 27 X_0 in the absence of sufficient (dense) modules and tungsten plates. We refer to these setups as "CERN setup I" and "CERN setup II" respectively, and figure 11 shows schematics of these two configurations. The range of energies explored, and amount of data taken, were approximately equal for both configurations, with around 4 days being available to test each configuration.

The geometry of these three setups were reproduced in GEANT4, as described in section 3.4. That section also gives more details of thicknesses of the various components.

2018 JINST 13 P10023

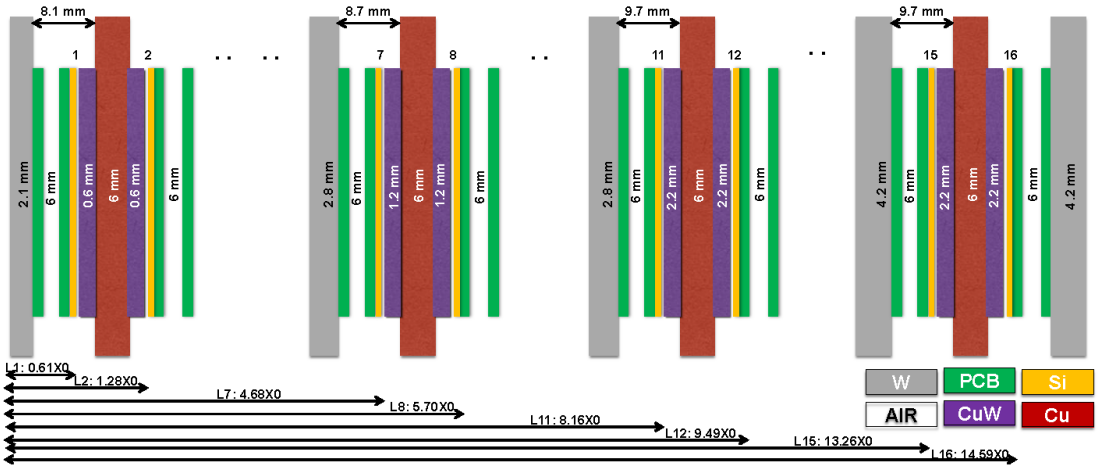

Figure 10. The experimental setup used at FNAL: eight double-sided modules mounted on copper cooling plates, separated by varying thicknesses of tungsten absorbers. The total thickness was just under 15 X_0. For clarity only half of the layers are shown.

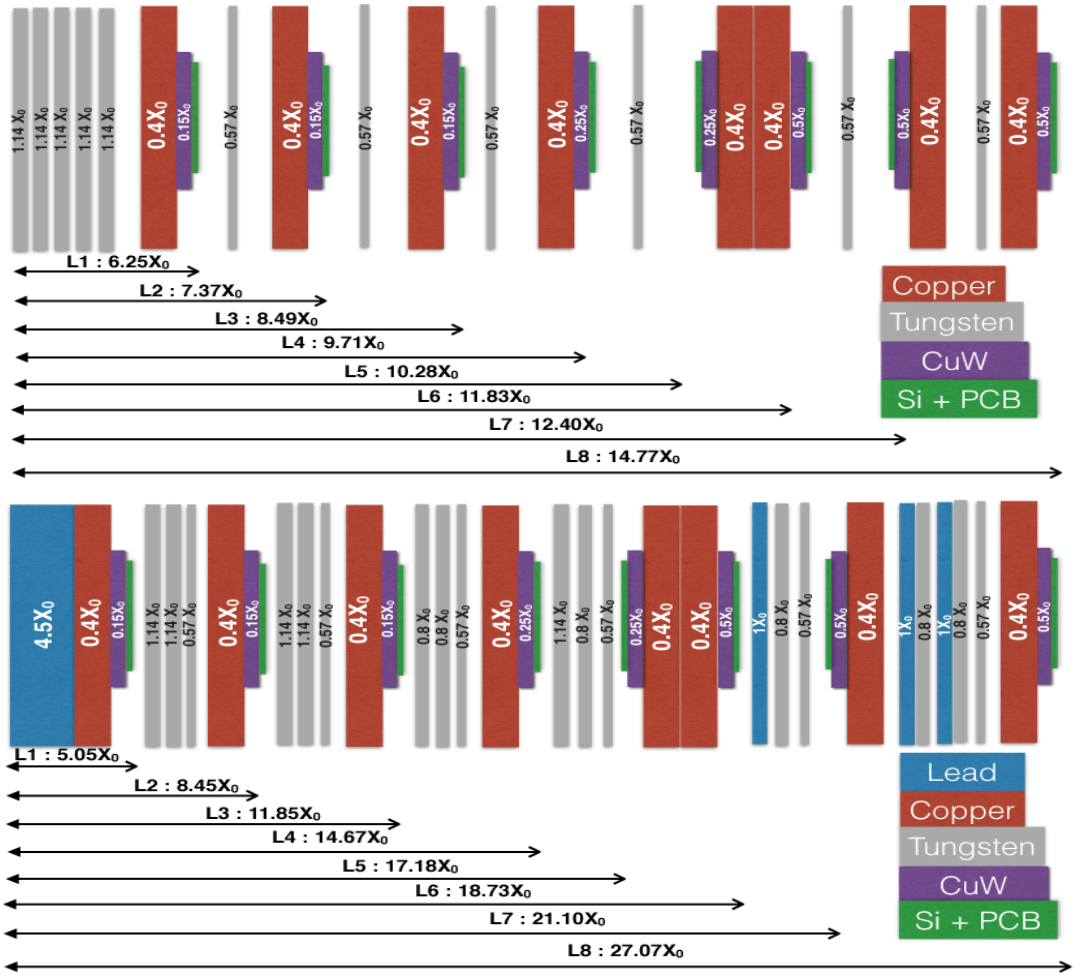

Figure 11. Setups I (top) and II (bottom) explored at CERN.

2018 JINST 13 P10023

3.2 Data taken

The particle beams available at FNAL and CERN were rather different and complementary, particularly for electrons. At FNAL the electron energies ranged between 4 GeV and 32 GeV, with the purity decreasing with energy to about 10% at the highest energies. Electrons were selected based on energy deposits in the silicon; the resulting "offline" electron purity, verified with simulation, was estimated to be greater than 97% with 95% pion rejection. The energy spread of the electrons in the FNAL beams was 3–5%, from the lowest to highest energies. At CERN, the electron purity was always higher than 98% and increased with energy. Electrons with energies between 20 GeV and 250 GeV were studied at CERN, with sub-percent spreads on the energies.

In addition to electrons, data were taken with 125 GeV protons at FNAL, whilst at CERN we had incident 125 GeV negative pions as well as muons. These latter were produced from 125 GeV π^- decays and thus had a range of energies.

Table 2 summarises the data taken at both FNAL and CERN, with 5–100 k events at each energy/particle data point. The rate capability of the DAQ chain was around 30–40 Hz. In addition to "physics" runs, data were taken when the beam was not present, in order to estimate pedestals, noise and stability, as described in subsequent sections.

Table 2. Data taken at FNAL and CERN in 2016.

	e^-												π^-	p^+	μ^-
Energy (GeV)	4	6	8	16	20	24	32	70	100	150	200	250	125	120	30–120
FNAL	X	X	X	X	X	X	X							X	
CERN					X		X	X	X	X	X	X	X		X

3.3 Triggering and particle selection

At both FNAL and CERN the main trigger source was plastic scintillators. At FNAL a single 2×2 cm^2 scintillator was used, with two SiPMs as readout devices in coincidence. At CERN two consecutive scintillators with PMT readout were used in coincidence, with the one closest to the detector defining the trigger size, at 4×4 cm^2. The CERN beamline also contains delay wire chambers (DWC), located at about 1.5m and 2.7m upstream of the HGCAL setup. These DWC measured the trajectory of the beam particles with an accuracy of about 1mm, and were used for the spatial precision measurements described in section 5.3.

3.4 Simulation framework

The various setups described in the previous section were simulated with GEANT4 [9] in the framework of the standard CMS software (CMSSW [10]). The materials upstream of the test setups were taken into account as much as possible as these can play a role, especially in the energy scale and transverse spread of incident electrons. At FNAL the main upstream components were 2 Cerenkov detectors and several scintillation counters, giving a total radiation length of 0.6 X_0 spread over 35 m. At CERN, the upstream material comprised 6 gas-filled wire chambers and 6 scintillation counters, giving a total radiation length of 0.27 X_0 spread over 15 m. Interactions further upstream would mostly result in the particle being diverted away from the trigger area.

2018 JINST 13 P10023

Table 3 shows the various materials and their thicknesses in the simulation. Whilst the thicknesses of all materials in the test setups were known with very good accuracy ($\simeq 0.1$ mm), the distances between the active layers and absorber layers could only realistically be measured to a precision of about 1 mm.

Table 3. Materials and their thicknesses in the GEANT4-based simulation.

Material	Thickness (in mm)	X_0
Tungsten	2, 2.8, 4	0.57, 0.8, 1.14
Lead	5.6, 25.2	1, 4.5
Cu cooling plate	6	0.4
CuW base plate	0.6, 1.2, 2.2	0.15, 0.25, 0.5
PCB	2×0.5	—
Si	0.2 mm active layer and 0.1 mm passive layer	—

In the hexagonal silicon sensor, only full hexagonal cells and half-hexagon cells were simulated. The mousebites at the sensor corners were not simulated and not used in any analyses. As these account for a small area at the edges of the sensors, far away from the bulk of the shower, the impact on performance was negligible. The full and half-hexagonal cells were the only active elements in the simulation.

To be able to mimic the test beam setup as closely as possible, we also took the beam momentum and lateral spreads ($\simeq 1\%$ and $\simeq 1$ cm) from the data and reproduced them in the simulation.

We simulated events with three different physics lists: FTFP_BERT_EMM, QGSP_FTFP_BERT_EML and QGSP_FTFP_BERT. The closest match was FTFP_BERT_EMM, as also used by CMSSW.

In simulation, the energy and incidence position of the beam were stored, as well as the raw energy deposits in the silicon cells.

The front-end electronics chain was not included in the simulation. In particular, noise was not added to the simulation, as the comparisons with data were made for relatively large signals where the effects of noise were negligible.

3.4.1 Silicon energy deposits: data vs. simulation

As described in section 4.2, the "standard candle" for silicon sensors is the minimum ionizing particle, "MIP". This is the most-probable energy deposit for a normally-incident minimum-ionizing particle. In reality the MIPs were approximated by incident high-energy hadrons or muons. These were simulated and the most probable energy deposit in the 200 μm active silicon thickness was estimated to be about 52 keV. We used this value when comparing energy deposits in data and simulation. We generally express energy deposits in the silicon in terms of MIPs in the remainder of this paper.

3.5 The data analysis framework, data preparation and reconstruction

A CMSSW-based offline event reconstruction and analysis framework was developed for the HGCAL beam tests in 2016.

2018 JINST 13 P10023

The software accepted raw data collected by the HGCAL DAQ. For each event this included a timestamp, trigger number, and the high- and low-gain ADC counts from 64 electronic channels from each Skiroc2 ASIC.

Firstly, each electronic channel was mapped to the cells of the sensors using a look-up table. Each cell was uniquely identified by a set of fields, together referred to as the "Detector ID". These fields were the layer number (only sensor layers were counted), the sensor number in the layer (in 2016 all layers had a single sensor: future tests will include multiple modules per layer), the two-dimensional local co-ordinate of the cell and a cell type identifier, which indicated if a cell was a full hexagon, half-hexagon, etc. From the Detector ID it was also possible to extract the position of the centre and the vertices of a cell in the laboratory Cartesian coordinate reference frame.

The result of the first step of the analysis sequence was to create an intermediate data structure, referred to as DIGIs, which contained per event the high- and low-gain ADC counts assigned to the corresponding Detector IDs. This RAW→DIGI step was commonly referred to as "unpacking". The DIGIs were directly used to evaluate the pedestal level of each cell from dedicated runs taken without beam.

After creation of DIGIs the final step involved the creation of a data structure, "RECO", which assigned energy deposited in units of MIPs to the corresponding Detector IDs. This DIGI→RECO process included pedestal subtraction and common-mode (CM) removal. Indeed, single MIPs could only be reconstructed by removing this CM noise on an event-by-event basis for each cell type.

Detailed studies of the pedestals and the noise are presented in section 4.1.

When assigning the estimated energy to a detector ID, a choice was made whether to use the high gain or the low gain ADC counts. In events with energy deposition in a cell above a certain value, non-linearities were observed in the high-gain ADC. For these the low-gain ADC counts were used to estimate the energy deposited. A detailed evaluation of this gain switching was performed, the results being presented in section 4.3. Finally the ADC→MIP conversion factors were needed. These were estimated from the single-particle response curves in a cell of the detector. For the beam tests at FNAL this calibration was performed with 125 GeV protons. Due to paucity of time the calibration was performed per layer. At CERN the calibration was performed per Skiroc2 using 125 GeV pions. The detailed studies of the single particle calibration can be found in section 4.2. Since protons and pions at the energies mentioned were not strictly minimum ionizing (500 MeV muons), the obtained single particle response was suitably corrected using inputs from simulation.

The energy E_i of cell i in an event may therefore be expressed in MIP units as:

$$E_i(\text{MIPs}) = \frac{\text{ADC}_i - \text{Pedestal}_i - \text{CM}_i}{(\text{ADC} \rightarrow \text{MIP})_i} \tag{3.1}$$

where Pedestal_i and CM_i are the pedestal and common-mode fluctuation for channel i. More details on these quantities are given in the next section. The energy for each channel as obtained above were termed "RecHits". To evaluate the CM noise only RecHits having energy lower than 2 MIPs (pre-CM-subtraction) were considered, to minimize contamination due to real signals. For reconstructing energy deposited in a detector layer the 2 MIP threshold was used as a lower limit, to minimize noise contamination.

The RecHits were the starting point for all analyses but some basic clustering was also performed to simplify some higher-level analyses such as energy response and resolution, as described in

2018 JINST 13 P10023

section 5.2. For each layer the energies in 1, 7 and 19-cells were stored, centered around the cell with the highest energy, as well as the total energy in a given layer (not counting the half-hexagons and mousebite cells at the sensor edges).

A visualization tool was developed to provide fast feedback and basic "event displays", by plotting the RecHits in the corresponding cells of a sensor for all the sensors in the setup. Figure 12 shows two such event displays for a 32 GeV electron event in the 16 layer setup at FNAL and that of a 250 GeV electron in the 8-layer setup II at CERN.

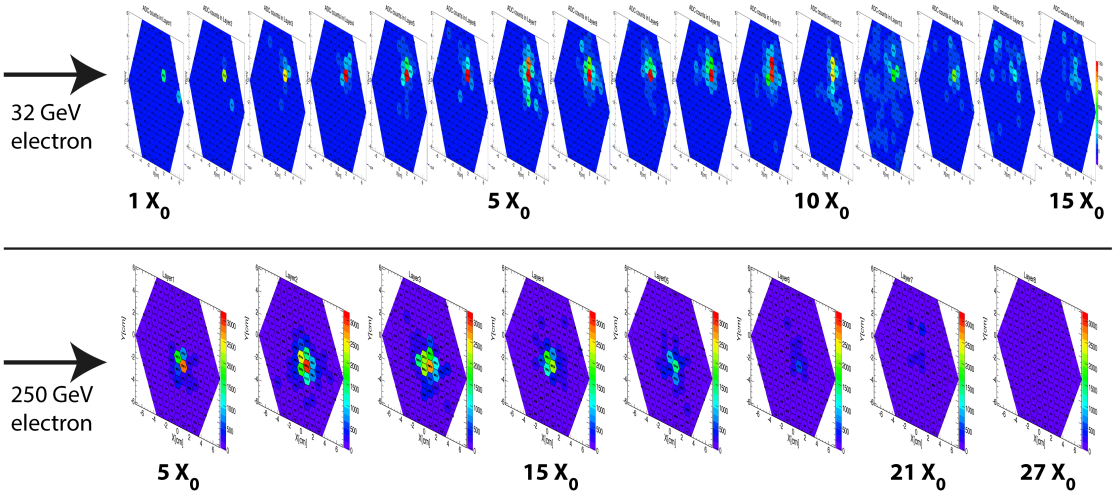

Figure 12. Event displays of the energy seen in each cell of consecutive silicon layers due to electron-induced electromagnetic showers. Top: FNAL test with 16 layers and 32 GeV electrons; Bottom: CERN test with 8 layers and 250 GeV incident electrons. The colour scale represents the amplitude of the RecHits in the cells in ADC counts.

4 Stability and calibration

4.1 Pedestal and noise: values and stability

Runs without beam were used to evaluate the pedestals and noise for each channel. The mean of the ADC-counts distributions defined the pedestal values, while the RMS of these distributions gave an estimate of the total noise for each channel. Files of the pedestal and noise values were created and used in analyses. We also evaluated the stability of these quantities with time.

The total noise, $\mathrm{RMS}_{\mathrm{total}}$ was the quadratic sum of the intrinsic noise of the channel, $\mathrm{RMS}_{\mathrm{intrinsic}}$, and any common-mode noise, $\mathrm{RMS}_{\mathrm{CM}}$ that may have been present in the system.

$$\mathrm{RMS}_{\mathrm{total}} = \mathrm{RMS}_{\mathrm{intrinsic}} \oplus \mathrm{RMS}_{\mathrm{CM}} \tag{4.1}$$

The total noise in the modules tested in 2016 (unirradiated silicon) was dominated by the electronic noise in the Skiroc2, which depended on the capacitance of the silicon cell to which it was connected. This is demonstrated in figure 13(left), which shows the total noise and intrinsic noise (expressed in ADC counts) as a function of the cell size. It can be seen that there was a strong correlation between the cell area and the total noise, suggesting that the CM noise was a function

2018 JINST 13 P10023

of the cell capacitance. Once the CM was removed, the intrinsic noise still showed a correlation with the cell area, as expected, although other sources of noise within the Skiroc2 dominated. Also shown, on the right of the same figure, is the stability of total noise with time during one running period in 2016.

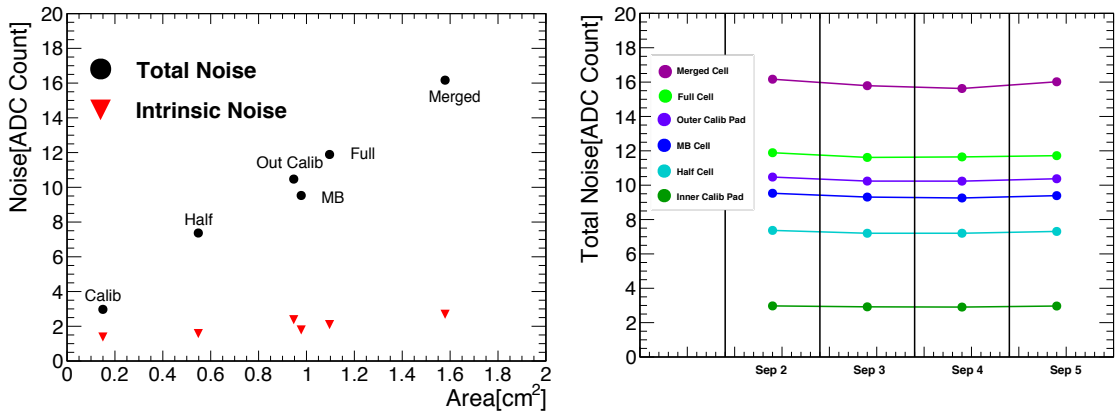

Figure 13. Left: total noise and intrinsic noise as functions of cell area for one of the Skiroc2s from the CERN test beam data. The total noise from all cells of each type has been averaged. Right: the total noise (averaged for each cell type) is shown as a function of time for one typical Skiroc2.

The intrinsic noise was evaluated, on an event-by-event basis, as the normalized "alternate sum" (AS) of the pedestal-subtracted ADC counts seen in N cells (of a given type), as shown in equation (4.2). This removes any common-mode fluctuations present in all cells.

$$\mathrm{RMS_{intrinsic}} = \left|\Sigma_{i=1}^{N}(-1)^i \times (\mathrm{ADC}_i - \mathrm{Pedestal}_i)/\sqrt{N}\right| \tag{4.2}$$

The RMS_{CM} was evaluated, again on an event-by-event basis, as the absolute value of the normalized subtraction of the AS from the "direct sum" (DS) of the pedestal-subtracted ADC counts seen in N cells (of a given type), as shown in equation (4.3):

$$\mathrm{RMS_{CM}} = \sqrt{\mathrm{DS}^2 - \mathrm{AS}^2}/N \tag{4.3}$$

where, DS and AS were evaluated as:

$$\mathrm{DS} = \Sigma_{i=1}^{N}(\mathrm{ADC}_i - \mathrm{Pedestal}_i); \qquad \mathrm{AS} = \Sigma_{i=1}^{N}(-1)^i \times (\mathrm{ADC}_i - \mathrm{Pedestal}_i) \tag{4.4}$$

In the systems at FNAL and CERN in 2016 we found that the total noise was dominated by RMS_{CM}. Attempts were made to identify and eliminate the source(s) of the CM noise. It was found to be entering through the bias-voltage lines of the modules but, despite the addition of filters, the CM could not be elliminated completely. Subsequent laboratory investigations pointed towards ground loops in the DAQ chain that required redesign for total elimination. Nevertheless, the CM noise could largely be removed on an event-by-event basis in the analysis.

Figure 14 shows, for one example channel in each Skiroc2 of the CERN 8-layer setups, the pedestal variation with time, as well as the intrinsic noise, for all channels for all the Skiroc2s. Both pedestal and noise were stable within 2 ADC counts, around ten times smaller than the signal from a MIP (see section 4.2) and negligible compared to shower signals (tens to hundreds of MIPs).

2018 JINST 13 P10023

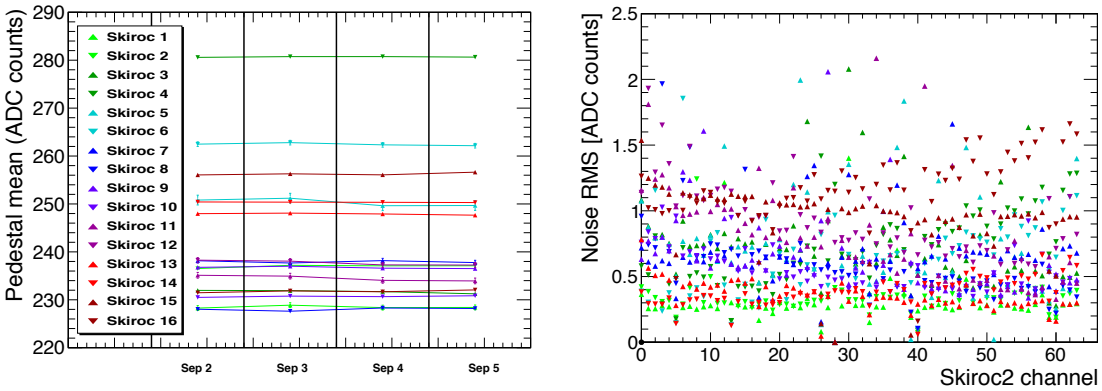

Figure 14. For all the Skiroc2s in the 8-layer configuration at CERN tested in September 2016: left — pedestal value for channel 20 as a function of time; right — intrinsic noise RMS as a function of channel number.

4.2 Calibration with single particles

Data taken with protons, pions and muons allowed the extraction of conversion factors from ADC counts (from the High Gain shaper, which was sensitive to small signals) to MIPs, and then to units of absolute energy. The ideal situation would have been to obtain a calibration constant for each cell. The transverse sizes of the beams, and scintillators used to trigger the prototypes, were too small to cover the full sensor area and there was not sufficient time to scan the full areas by moving the prototypes. We could calibrate several cells per sensor, study their uniformity and use averages as the estimate for the other cells in the same Skiroc2 (for the CERN calibration) or in the whole sensor (pair of Skiroc2s, for the FNAL data).

However, in addition to the dedicated pion beam runs at CERN, we also took advantage of a period of operation of the NA61 [11] experiment, about 40m upstream of our prototype. During NA61 operation there were residual muons spread over a wide area that passed through our detector. We replaced our standard trigger scintillators with a $10\times10\,\mathrm{cm}^2$ device, which enabled us to calibrate many more sensor cells.

For this paper we concentrate on the CERN measurements, which were more extensive than could be performed at FNAL due to time constraints.

Figure 15(left) shows an example of the energy distribution obtained in a typical channel for the pion runs. The left peak corresponds to the pedestal and the right to the MIP signal. In addition to the single-MIP peak at around 18 ADC counts, a small double-MIP peak is evident at around 36 ADC counts. These histograms were then fitted with a sum of a Gaussian distribution and two convolutions of Landau and Gaussian distributions. The Landau parameters (MPV — most probable value, and sigma) were free; the widths of the signal Gaussians were both constrained to have the same width as the pedestal Gaussian, whilst their MPVs were allowed to float. The inter-cell calibration constants were extracted from the peaks of the first Landau+Gaussian convolution.

Only those cells covered by the small-area pion beam could be calibrated in this way — about 16 central cells per modules. In order to calibrate more of the cells, we used a larger trigger scintillator with a disperse muon beam, covering about 100 cells per module. However, the S/N for any given cell is much reduced, as demonstrated by figure 15(middle), where the fit fails to

2018 JINST 13 P10023

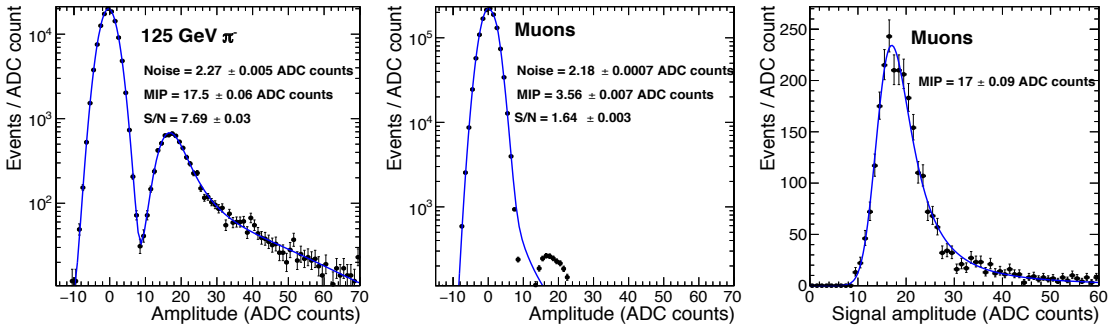

Figure 15. Left: distribution of the amplitude (pedestal-subtracted ADC counts) of a typical channel in the first layer of the CERN prototype for runs with a pion beam. The amplitude is fitted with a sum of a Gaussian (for the pedestal) and two convolutions of a Landau distribution and a Gaussian (for the 1-MIP and 2-MIP signals). Middle (resp. Right): distribution of the amplitude of the same channel for a wide-area muon beam, without (resp. with) using the tracking procedure.

converge. To increase the effective S/N for these cells we took advantage of the high granularity and intrinsic tracking capability of the prototype calorimeter, which allowed the reconstruction of the trajectory of the muons, and then the selection of only the cells with a MIP signal. The procedure is described by the following sequence:

- Pedestal and common-mode noise were subtracted from raw data, as described in section 4.1.
- Only cells with MIP-like signals were retained: cells with energy lower than 9 ADC counts[3] (~0.6 MIPs) were dropped, as well as those with energy higher than 62 ADC counts (~4 MIPs).
- A least-squares linear fit was made to the hits to evaluate the particle trajectory.
- The distances between the hits and the reconstructed line were computed. The hits, at a distance larger than 2 cm from the line were dropped. This allowed the rejection of any remaining spurious hits (from noise).
- The remaining hits were then used to define a reconstructed track.

The energies of the hits belonging to a track were then used to fill histograms of MIP signals. These histograms were fit with a convolution of a Landau distribution and a Gaussian, as demonstrated in figure 15(right), when the number of entries was at least 200. The MIP calibration constants were then extracted from the maxima of the fits, as for the simpler method.

Figure 16 shows the MIP calibration constant and S/N for the calibrated cells, as a function of Skiroc2, after applying the tracking procedure. The calibration pads show higher MIP values compared to other pads in the same Skiroc2. This was due to the lower capacitance of these cells compared to the larger full hexagons. The higher capacitance of the full hexagons, coupled with the Skiroc2 input impedence, lead to a slower rise-time than for the calibration cells, which, when shaped in the Skiroc2, in turn lead to a ballistic deficit [12] and thus lower relative amplitude for

[3]The intrinsic noise was about 2 ADC counts in most of the cells.

2018 JINST 13 P10023

the full hexagons. As the noise was also slightly lower for the calibration cells — again due to the lower capacitance — the overall S/N was significantly larger, as expected.

Table 4 presents the fraction of calibrated cells when using the standard procedure and the tracking technique.

Figure 17 presents the average values of the MIP calibration constants and S/N as functions of the Skiroc2 number, for the three types of run dedicated to the calibration at CERN. The trend with the Skiroc2 number shows that at least one calibration constant was required per ASIC. The vertical error bars represent the RMS of the calibration constants for all cells calibrated within the specific Skiroc2 ASIC.

The effect of using these optimized calibration coefficients for energy measurements, instead of a constant value or smeared values, is discussed in section 5.2.

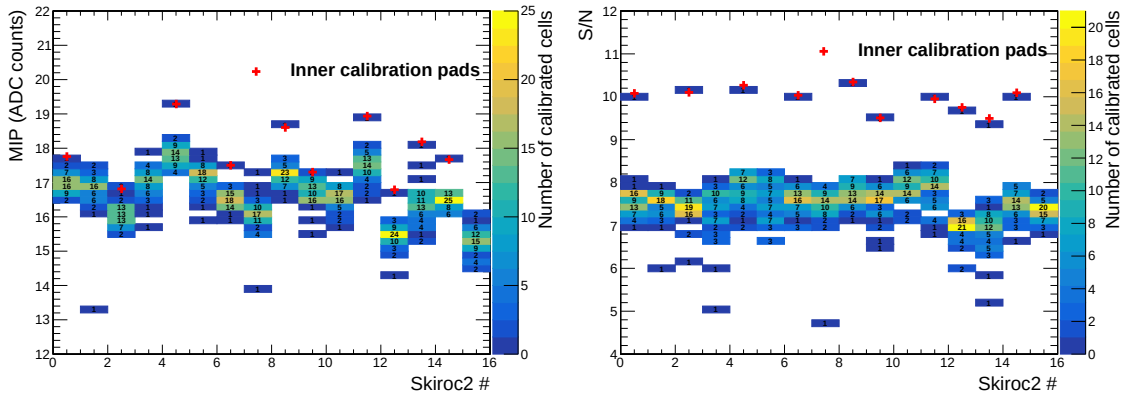

Figure 16. MIP value (left) and S/N (right), for calibrated cells, as a function of the Skiroc2 for the CERN tests. These values were obtained using the tracking procedure, using the runs with beams of muons with large trigger scintillator. The red crosses represent the calibration cells of the sensors.

Table 4. Fraction of calibrated cells (CERN data).

	Fraction of calibrated cells	
Run type	Standard procedure	Tracking procedure
Pions	17%	22%
Muons with standard trigger scintillator	17%	22%
Muons with large trigger scintillator	28%	77%

4.3 Gain calibration

As discussed in section 2, the Skiroc2 features dual-gain amplification: "high gain" (HG) for silicon signals up to about 100 MIPs, with a good S/N ratio for single MIPs (used for the inter-cell calibration described in the previous section) and "low gain" (LG) for signals up to about a thousand MIPs, but with a poor S/N ratio for single MIPs. The signals from both HG and LG were digitized and read out for each event. The analysis then selected the most appropriate gain determined by the signal size. In order to evaluate the crossover point (the threshold above which it is advantageous to use the LG instead of HG) we compared the signals from the two gains after pedestal and common-mode

2018 JINST 13 P10023

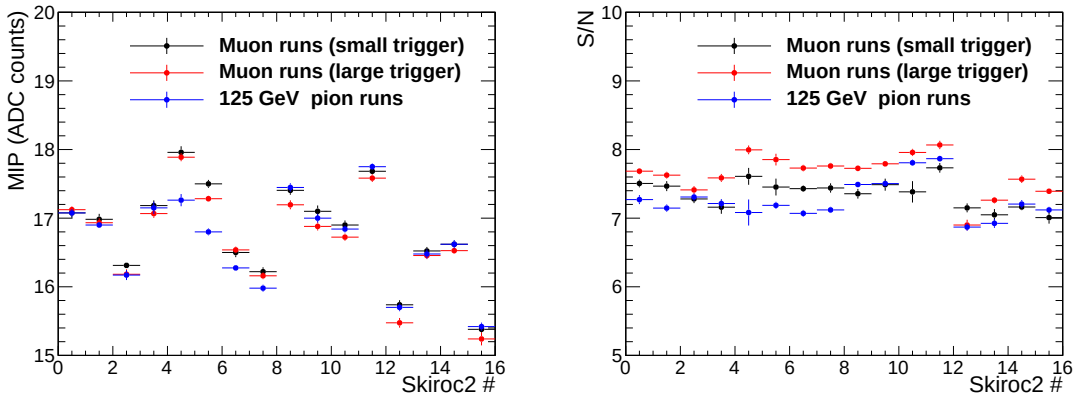

Figure 17. Average MIP peak (left) and S/N (right) as a function of the Skiroc2.

subtraction, on an event-by-event basis. We used electrons of different energies to explore the full dynamic range (E_e = 20, 70, 100, 150, 200, 250 GeV) and for the two Skiroc2 chips per module separately. The output of the study was a set of two-dimensional histograms showing the expected linear trend between the two gains and the crossover point around the position [HG ; LG] = [1800 ; 200] ADC counts, above which the HG shaper saturates.[4] In order to have a precise measurement of the relative slope, defined as the ratio between the HG and LG at the crossover point, we performed linear fits in two different LG ranges: 0–150 and 250–400 ADC counts. The HG saturation point was extracted by interpolating the two lines and finding the intersection point. The error on the intersection point was then evaluated by propagating the fit uncertainties accordingly.

An example of the HG-LG correlation plot for E_e = 250 GeV electrons is shown in figure 18. The LG and the HG cut off, extracted from the fit of the HG-LG correlation plot for each layer are presented in table 5 for the first Skiroc2 as an example. Consistent results were found for the second Skiroc2 chip. For each layer and Skiroc2 we calculated the gain ratio, defined as the ratio between the HG cut off and the LG cut off (HG/LG), which was used to normalize the signal response. Results on the gain ratio for the first Skiroc2 are reported in table 5. As can be seen from the table, there were no significant trends nor discrepancies found for the gain ratio for the 8 layers and the average value of the ratio of around 10 was expected by the ASIC designers. Also, the gain ratio was independent of the beam energy and Skiroc2.

5 Measurements of shower shapes, energy and position

5.1 Longitudinal and transverse shower shapes

One of the main goals of the 2016 HGCAL beam test was to verify the GEANT simulation of the complete system that is used to evaluate its overall performance and tune the design of the final detector. One of the key aspects of such simulations, especially for the HGCAL, is the reproduction of the longitudinal and transverse shower shapes over a wide range of energies. The eight-layer setups used at CERN were used for this evaluation.

[4] Although the shaper saturates, it is a "soft" saturation, where the output can continue to increase but with an incorrect gain and increased non-linearity. It is not a strict cutoff, such as with an ADC saturation.

2018 JINST 13 P10023

Table 5. High Gain (HG) and Low Gain (LG) cut-off values and the fit results on the gain ratio, evaluated for each of the 8 layers for the first Skiroc2 chip in the CERN setups.

Layer	LG cut off	HG cut off	Gain Ratio (HG/LG)
1	186.2 ± 0.2	1897.1 ± 1.1	10.0 ± 0.4
2	187.1 ± 1.7	1872.5 ± 16.3	10.0 ± 0.4
3	204.9 ± 0.9	1990.3 ± 7.4	9.8 ± 1.6
4	196.9 ± 1.0	1915.0 ± 8.4	9.7 ± 1.7
5	196.7 ± 2.0	1910.6 ± 18.4	9.7 ± 2.2
6	193.0 ± 3.2	1893.4 ± 30.8	9.8 ± 2.2
7	199.1 ± 1.4	1957.9 ± 13.0	9.8 ± 1.6
8	226.3 ± 0.8	2085.0 ± 5.4	9.2 ± 0.2

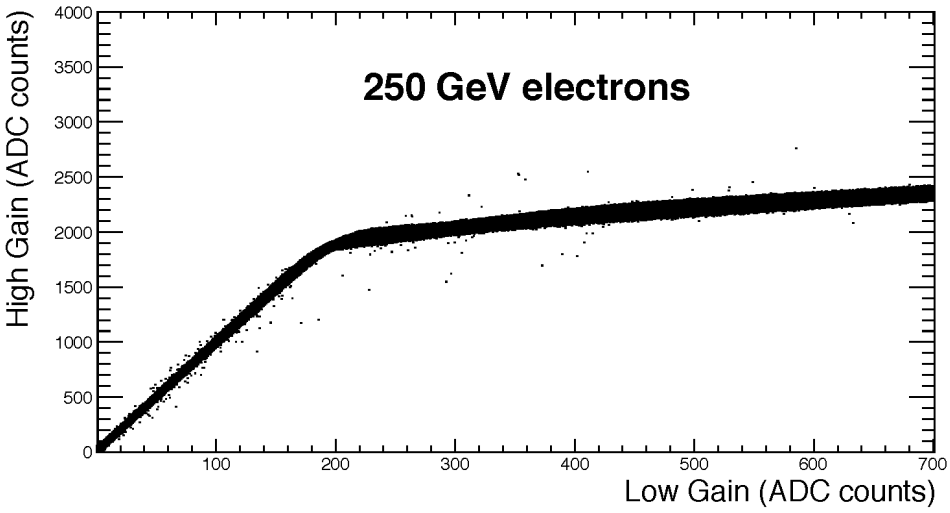

Figure 18. The High-Low Gain correlation for an incoming electron beam of energy $E_e = 250\,\text{GeV}$. The upper limit on the plot for LG of 700 ADC counts was simply to focus on the switching point.

We made a comparison between data and simulation based on the FTFP_BERT_EMM and QGSP_FTFP_BERT physics lists. The former is the one used by default in CMSSW for simulation of the complete HGCAL, whilst the latter is used in CMSSW for simulation of the homogeneous CMS crystal calorimeter.

5.1.1 Longitudinal shower shapes

The longitudinal depth barycentre, t, for two example electron beam energies for CERN setup II is shown in figure 19, and is defined as:

$$t = \frac{\sum_{i=1}^{8} \left(E_i X_{0,i}\right)}{\sum_{i=1}^{8} E_i}, \tag{5.1}$$

where E_i is the layer raw energy and $X_{0,i}$ the total calorimetric radiation length up to layer i. A good agreement between data and simulation is observed. At lower energies there is a small shift of the shower depth in the data to lower values compared to the simulation. This could be due to electron showering in not-simulated upstream material in the H2 beamline.

2018 JINST 13 P10023

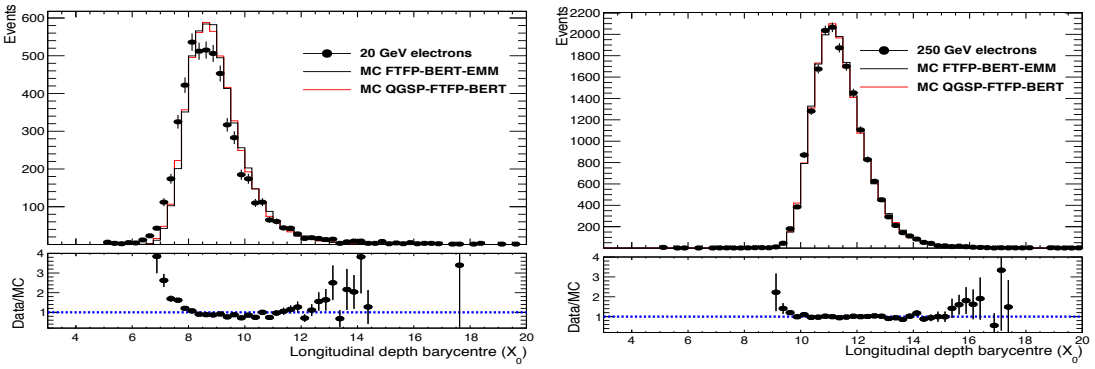

Figure 19. Longitudinal depth barycentre distribution comparison between data and simulation for electron energies of 20 and 250 GeV at CERN. The comparison was performed against two simulated physics lists: FTFP_BERT_EMM and QGSP_FTFP_BERT. The ratio plot was made using the FTFP_BERT_EMM physics list.

In order to test this supposition we plotted the fraction of energy deposited in the first layer with respect to the total energy deposited in all layers, as shown in figure 20. This variable is sensitive to early showering upstream of the calorimeter. In these plots a very small departure between data and simulation is observed, especially for the lower energies, reinforcing the supposition that there was a small amount of early showering in the H2 beamline in non-simulated materials.

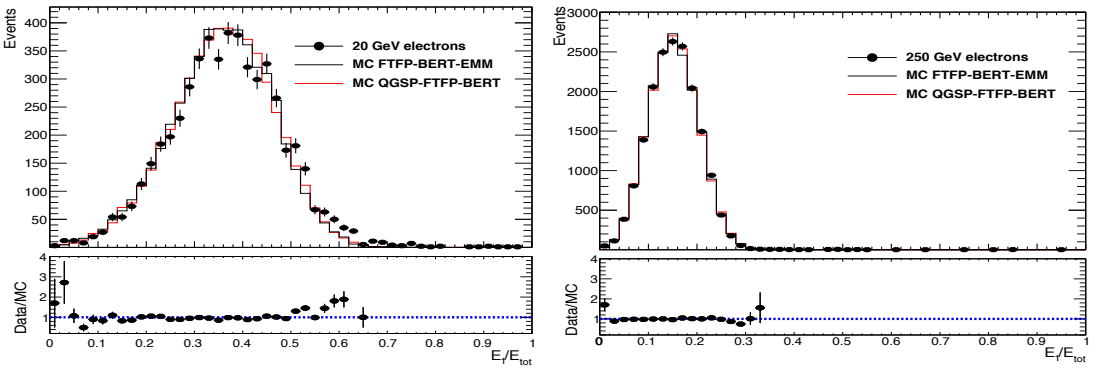

Figure 20. Fraction of energy deposited in the first layer for data and simulation for electron beam energies of 20 and 250 GeV. The ratio plot was made using the FTFP_BERT_EMM physics list.

The longitudinal evolution of the electromagnetic showers is shown in figure 21 for both FNAL and CERN data, as well as the simulations based on the FTFP_BERT_EMM physics list. For each beam energy, the total energy in each plane ($\text{Energy}_{\text{layer}}$) was evaluated and plotted at the appropriate longitudinal depth (expressed in X_0). The depth at which the fractional energy was highest represents the shower maximum position. It can be seen that the shower maximum moved deeper into the calorimeter as the beam energy increased, as expected. An agreement at the level of better than 10% was found between data and simulation.

2018 JINST 13 P10023

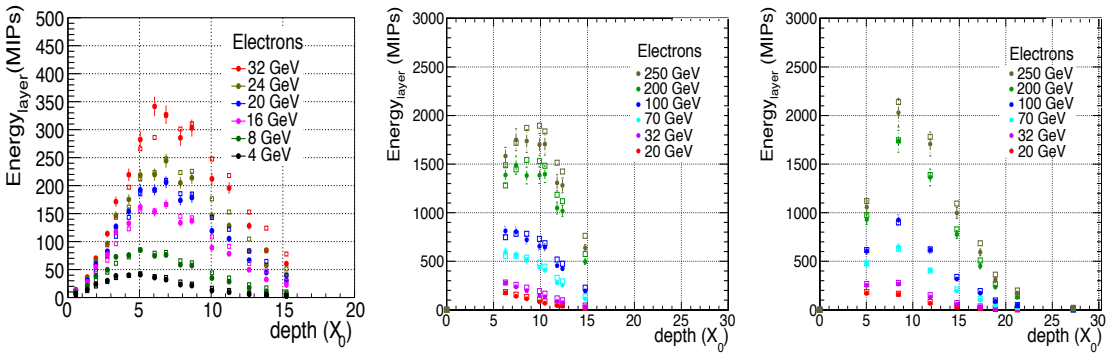

Figure 21. Longitudinal evolution of the electromagnetic showers as functions of electron energy: solid symbols represent data whilst the open symbols are for simulation. Left: for the 16-layer configuration at FNAL; Centre/right: CERN 8-layer setups I and II respectively.

5.1.2 Transverse shower profiles

In figure 22 a comparison of transverse shower profiles between data and simulation is shown for electrons incident on CERN setup I for two of the eight layers. Layer 2 was close to the shower maximum, whilst layer 6 was closer the longitudinal tail of the shower. The shapes shown are energy densities as a function of the radial distance from the seed cell. They were also normalized to the energy of the seed (shown in the first bin), a representation that, in principle, allows the parameterization of the lateral energy deposition as a function of shower depth and beam energy. A good agreement between data and simulation was observed, particularly for the core of the showers (the most energetic cells, nearest the seed), with very little difference between the FTFP_BERT_EMM and QGSP_FTFP_BERT physics lists.

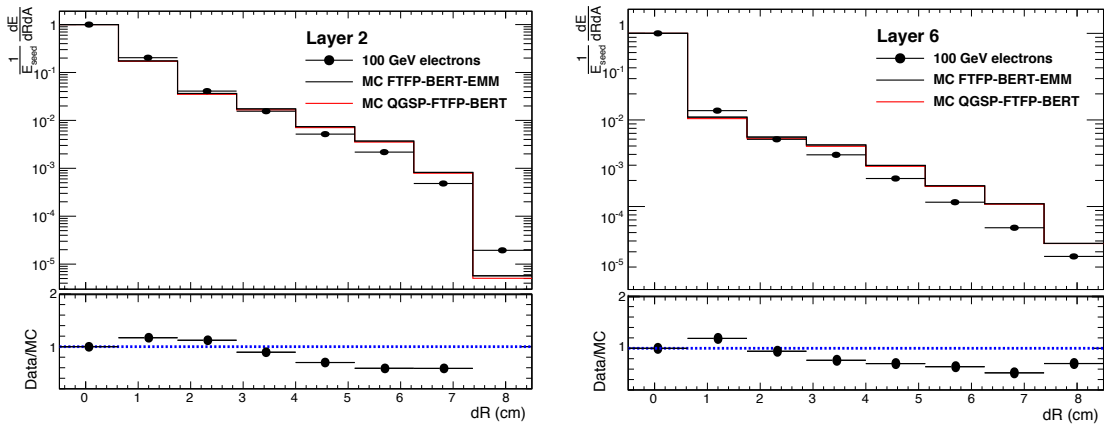

Figure 22. Transverse shower profile comparison between data and simulation for layers 2 and 6 in CERN setup I for 100 GeV electrons. The shapes shown are energy densities (energy per active area) as a function of the radial distance from the seed cell. They were also normalized to the energy of the seed. The ratio plot was made using the FTFP_BERT_EMM physics list. One point in the left ratio plot is off-scale.

Another method of estimating the transverse shower profile was to calculate the energy ratios between the central (seed) cells (E1) and the total energy in 7 (E7) or 19 (E19) cells. Figure 23 shows the distributions of E1/E7 and E1/E19 for layer 7 of CERN setup I for 100 GeV electrons,

2018 JINST 13 P10023

comparing to both of the simulated physics lists. A good agreement was found between data and simulation, particularly for the core of the showers. The other layers show similar agreements. FNAL and CERN setup II show similar results. No significant difference was seen between the two physics lists.

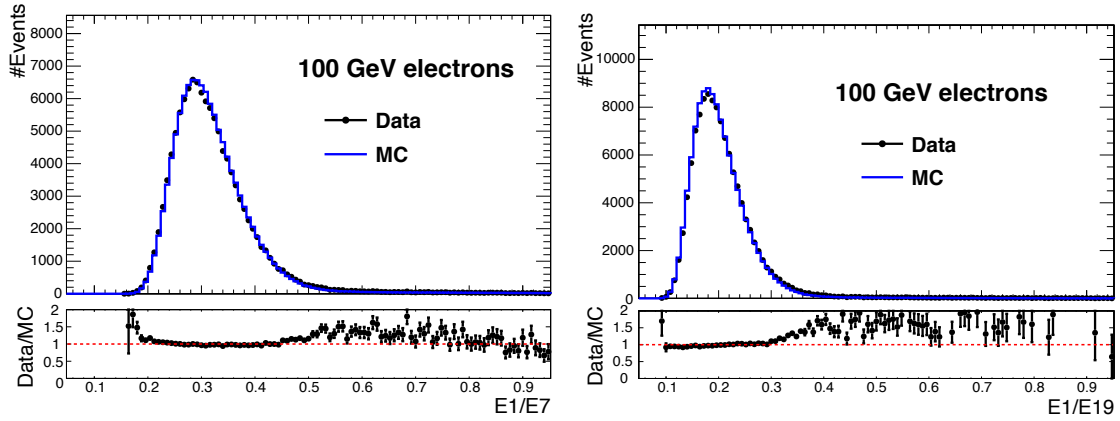

Figure 23. E1/E7 (left) and E1/E19 (right) for 100 GeV electrons in layer 7 of CERN setup I with simulation based on the FTFP_BERT_EMM physics list. Black markers are data and blue histogram is the simulation. The simulation is normalized to the number of events in data.

5.2 Energy measurements and resolution

RecHits were selected if their energy deposition exceeds a threshold of 2 MIPs , corresponding to ∼16 times the typical intrinsic noise in a cell. The energy deposited in each active layer was obtained by summing together the energy measured by all the selected RecHits, with the only exception being those in the non-hexagonal cells along the edge of the sensor, which exhibited larger noise occasionally and were excluded from the analysis.

For each event, the total energy measured corresponded initially to the sum of the energy reconstructed in the individual active layers. This energy reconstruction process was applied to both data and simulation for consistency.[5]

Figure 24 shows an example of the total energy measured in the active layers in units of MIPs, for the two 8-layer setups tested at CERN, as a function of the beam energy. Both data and simulation are shown.

The energy estimated in the simulation was about 15% above that measured in data. This offset was almost flat as a function of the energy and was observed also for the 16-layer setup at FNAL. This difference in the energy scale was found to be due to the choice of a GEANT4 simulation with the physics list FTFP_BERT_EMM [13], which was used as it gave the best agreement in shower shapes between data and simulation (see section 5.1). Other lists gave slightly better agreement for the overall energy scale, but did not describe the shower shapes as well.

As discussed above, one of the main goals of the 2016 beam tests was to probe the data-simulation agreement in the description of the shower development, while the recovery of the full energy scale of showering electrons was beyond the scope. It should also be noted that we were not

[5]Detector noise was not included in the simulation.

2018 JINST 13 P10023

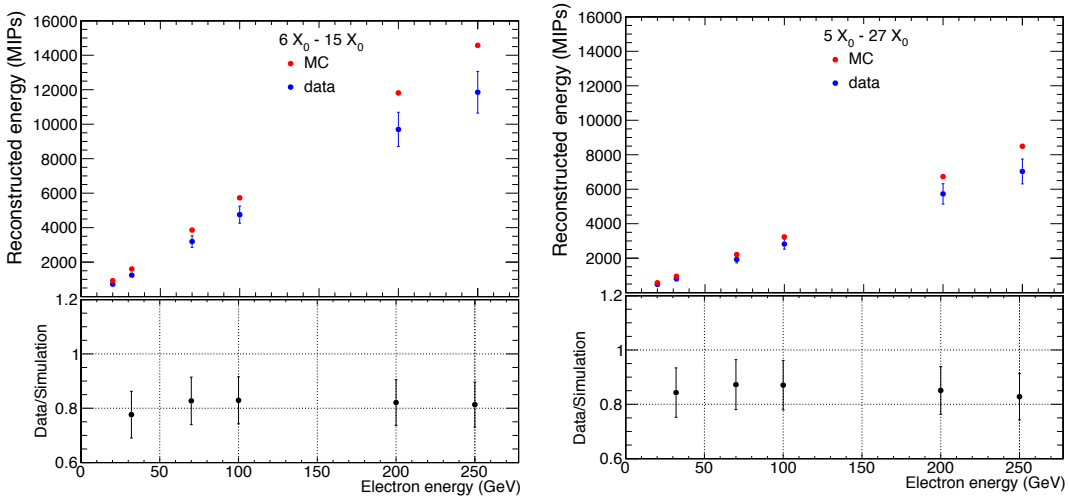

Figure 24. Non-weighted energy reconstructed in the active layers of the detector in data and simulation, for the two configurations at CERN, expressed in units of MIPs.

aiming to achieve the best possible energy resolution as the number of layers available was small. Since variables such as the lateral shower shapes and the relative energy resolution were unaffected by a global scale offset, a correction was performed on the simulation by reducing its measured energy by a factor 1.15, such that its global scale matched that of the data.

An example of the energy spectra for 100 GeV electrons, from both data and simulation, is given in figure 25, prior to the final absolute scaling mentioned above. The full shape is seen to have a reasonable agreement between data and simulation. The tails do not match perfectly. Part of this is likely due to the absence of noise in the simulation. There may also have been some small amount of pion contamination in the data, not removed by our cuts. To avoid the effects of the tails, for the resolution measurements in this paper we used a restricted-range Gaussian fit.

As discussed in section 3, the secondary beam used at FNAL to study the electron response was contaminated by a significant fraction of pions, with the pion fraction varying between 20–90% for beam energies ranging from 4–32 GeV. In order to select an electron event a threshold on the total energy reconstructed by the above procedure was applied. This was motivated by a study in simulation to ensure that less than a few percent of the selected events were due to interacting pions, as discussed in section 3.4. No such selection was needed for the CERN data due to the higher purity of the electron beams.

The setups tested at CERN and FNAL had active layers of silicon interspersed with absorbers of different thickness as described in section 3. In these configurations, to estimate the total energy deposited in the detector, the energy deposited in the absorber layers needs to be evaluated. With the assumption that the dominant energy loss was through ionization in the absorbers, the energy deposited in the downstream silicon layers could be used to estimate the total energy loss, $\text{Energy}_{\text{tot}}$, in N layers as:

$$\text{Energy}_{\text{tot}}[\text{MIP}] = \sum_{i}^{N_{\text{layer}}} \left(E_i^{\text{Abs}}[\text{MIP}] + E_i^{Si}[\text{MIP}] \right) \tag{5.2}$$

where E_i^{Abs} was the energy deposited in the absorbers immediately upstream of the silicon layer

2018 JINST 13 P10023

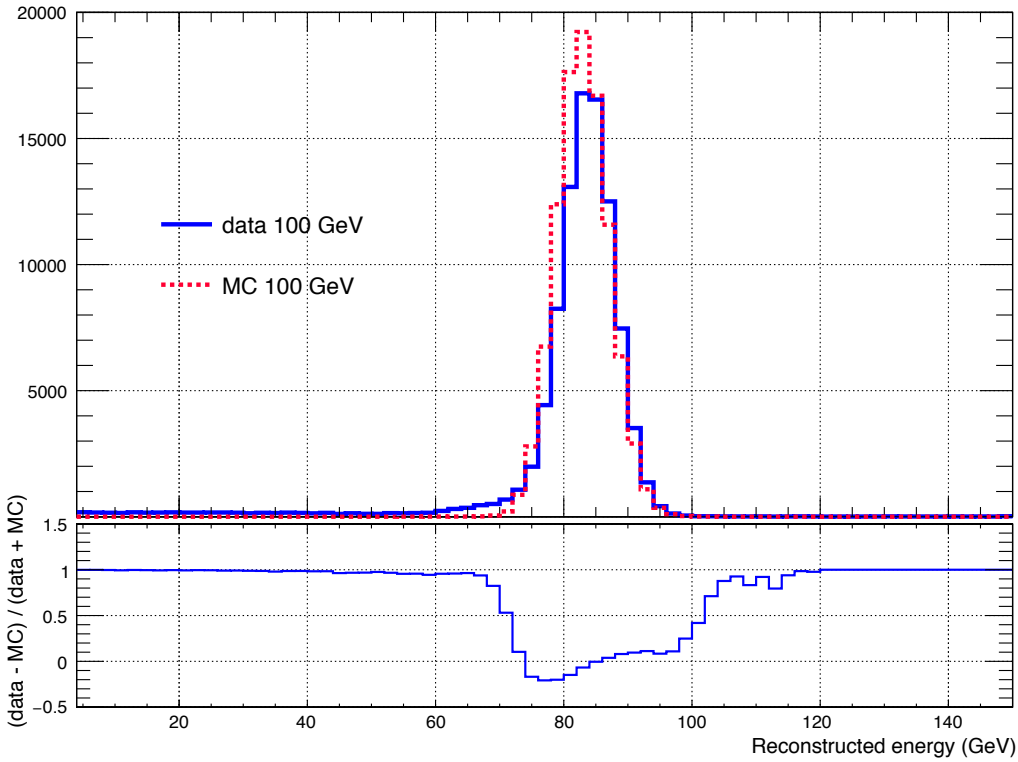

Figure 25. Energy spectra for 100 GeV electrons for CERN setup II, for data and simulation. The final absolute calibration has not been applied.

and E_i^{Si} was the energy deposited in the silicon, both expressed in units of MIPs. To estimate the energy lost in the absorber layers, sampling factors were calculated, reflecting the dE/dX for MIPs in the various absorbers. We assumed that the number of MIPs passing through a given absorber layer $E_i^{\mathrm{Abs}}[\mathrm{MIP}]$ was the average number of MIPs measured in the two adjacent silicon active layers $i-1$ (n_{i-1}^{Si}) and i (n_i^{Si}), as follows:

$$E_i^{\mathrm{Abs}}[\mathrm{MIP}] = \frac{n_{i-1}^{\mathrm{Si}} + n_i^{\mathrm{Si}}}{2} \, \frac{\Delta E_i^{\mathrm{Abs}}}{\mathrm{GeV2MIP}} \,, \tag{5.3}$$

where ΔE_i corresponded to the total amount of energy deposited by one MIP in the material $\left(\frac{dE}{dX}_i \times \Delta x_i\right)$ and GeV2MIP refers to the conversion factor discussed in section 3.4.

In a sampling configuration with N_{layer} layers, it can be shown that the combination of equations. (5.2) and (5.3) on average results in:

$$\mathrm{Energy}_{\mathrm{tot}}[\mathrm{MIP}] = \sum_i^{N_{\mathrm{layer}}} \left[(W_i + 1)\ n_i^{\mathrm{Si}}\right], \text{ with } W_i = 0.5 \cdot \left(\frac{dE}{dX}_i^{\mathrm{Abs}} + \frac{dE}{dX}_{i+1}^{\mathrm{Abs}}\right) \tag{5.4}$$

The weights W_i were computed using the PDG [14] values of energy loss for the absorber materials. This approach works well with thin absorbers and when ionization is the main process of energy deposition. It improved the estimated energy resolution by ≃20% over an unweighted estimate based simply on the energies measured by each silicon layer. Although this overall energy

2018 JINST 13 P10023

estimation (clustering and weighted sum) is not optimal, it serves the present purpose of making a reasonable comparison between data and simulation.

The obtained estimate in the number of MIPs was then converted into energy as discussed in section 3.4. This procedure was used to reconstruct the total energy deposited in the detector for each electron energy.

The effect of the accuracy of the MIP calibration constants was evaluated using the 250 GeV electron data. This energy was chosen since the stochastic term was smallest and effects contributing to the constant term — including the calibration — would be prominent. We compared energy estimates using the measured coefficients, or a constant value of 17 ADC counts/MIP, or the measured values smeared by 5%, 10%, 15% or 25%. The results are shown in figure 26.

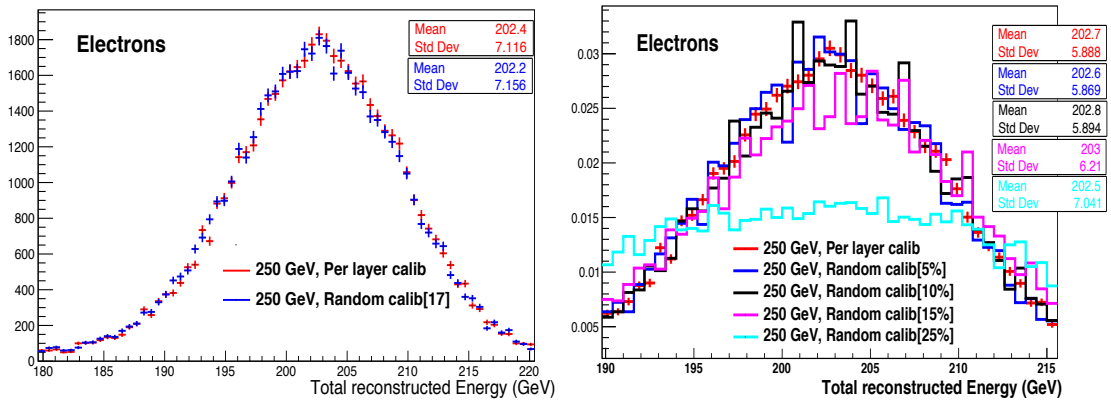

Figure 26. Left: effect of selecting a constant 17 ADC counts/MIP as the calibration constant for all 8 planes in the CERN 2016 beam test, on the reconstructed energy for incident 250 GeV electrons; right: effect on the reconstructed energy for incident 250 GeV electrons of smearing the measured calibration constants by between five and 25 percent on the 8 planes of the 2016 beam test. Note that for the right-hand plot the means have been normalized to the same value and the corresponding widths scaled accordingly.

There was no significant difference in shape or width of the reconstructed electron energy spectrum when the constant 17 ADC counts/MIP or smearings up to 10% were used. However, it should be emphasized that the stochastic term was still large, due to the small number of layers, so the effects of calibration coefficients were likely still present but dominated by sampling fluctuations.

The energy distributions were fitted with a Gaussian function within the range [mean - rms, mean + 2 rms], and the resulting mean and σ values were taken as the mean energy response of the detector at a given beam energy and the corresponding energy resolution.

Figure 27 shows the ratio of the measured response as a function of the electron beam energy. The difference from unity was due to non-complete energy containment in the relatively small setup. The error on the mean response in the data includes a conservative 5% systematic uncertainty in the single particle calibration that was added in quadrature to the statistical error obtained from the fit.

Figure 28 shows the measured energy resolution as a function of the electron beam energy and the estimate from the GEANT4 simulation. Results from the tests at FNAL and in CERN setup II are displayed together to emphasize the different sampling regimes of the two setups. The simulation is seen to match the data to better than ~4% for all energies.

2018 JINST 13 P10023

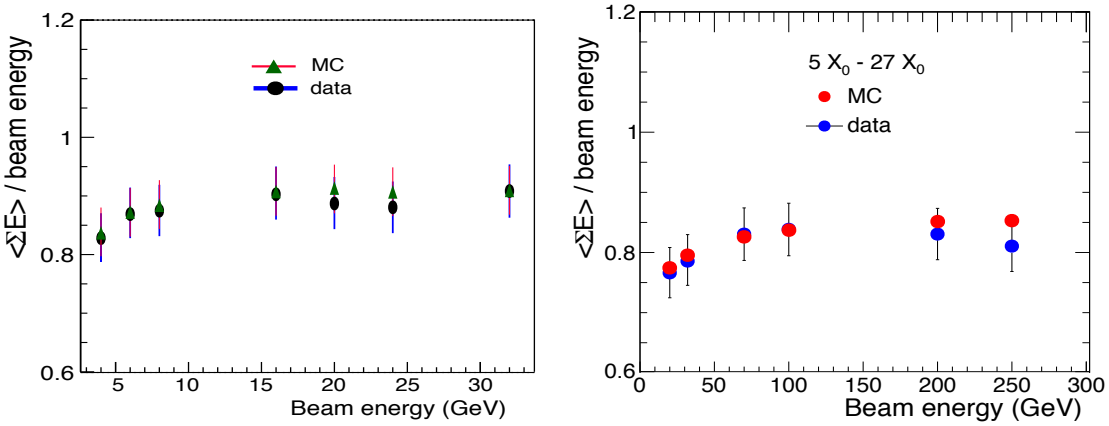

Figure 27. Ratio of the mean energy response to electron beam energy as a function of the electron energy in data and simulation, for the test at FNAL (left) and CERN setup II (right).

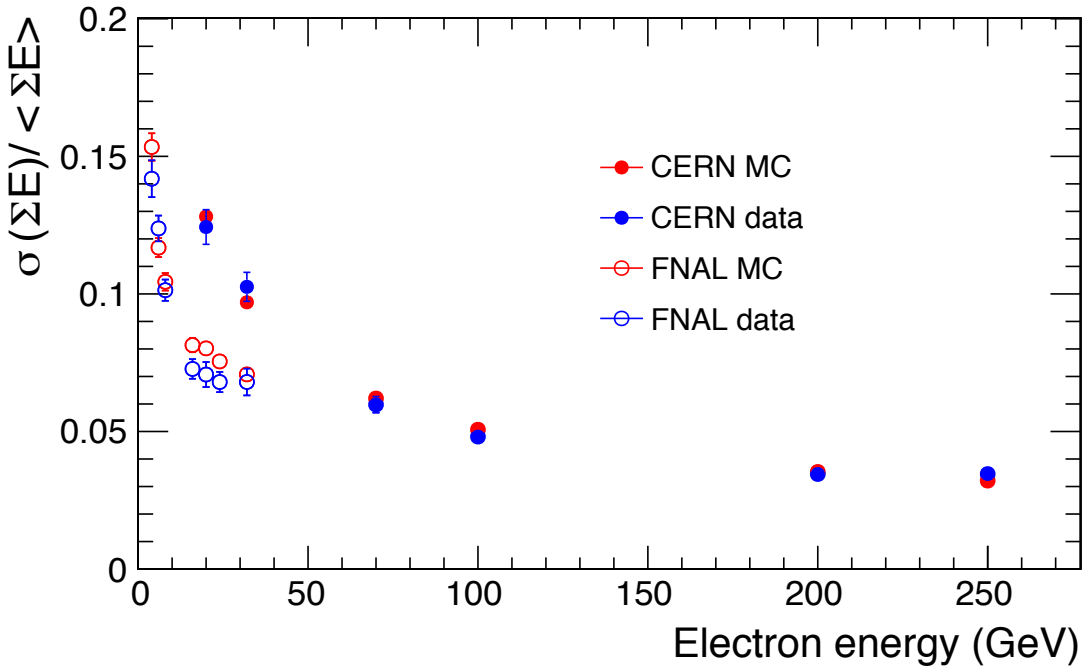

Figure 28. Relative energy resolution as a function of the electron beam energy in data and simulation, for beams at FNAL and CERN.

5.3 Position resolution

Accurate measurements of the incidence position and direction of showers are key inputs to the particle-flow[6] performance of the upgraded CMS detector. The prototype calorimeter's capability to localize electron-induced particle showers has been investigated using data from CERN setup I ($6X_0$–$15X_0$). Information on each cell's coordinate and deposited energy were used to reconstruct the shower main impact position on a sensor. Subsequently, residuals to external reference mea-

[6]"Particle flow" is the technique of estimating jet energies by combining information from all trackers and calorimeters, instead of simply having a weighted sum of calorimeter energies.

2018 JINST 13 P10023

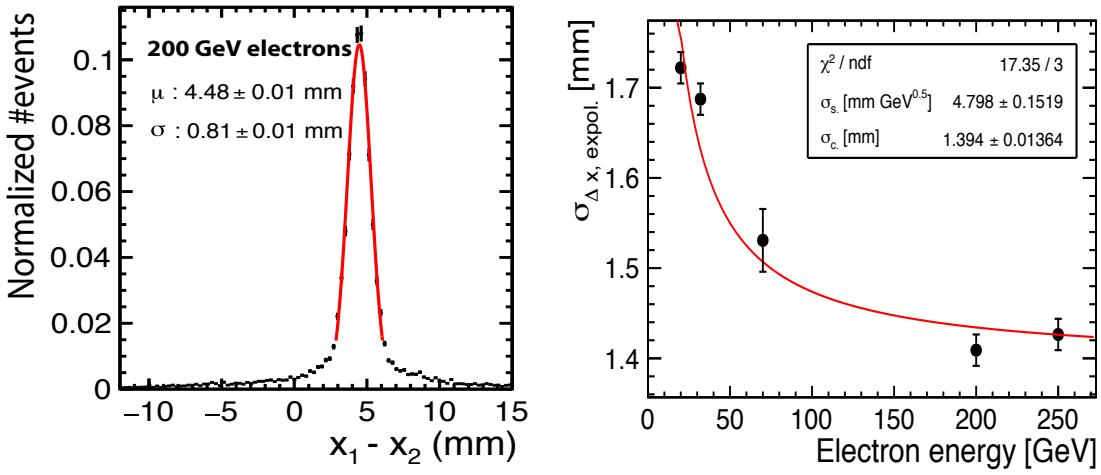

Figure 29. Left: the distribution of difference in X (horizontal) position measured by the two DWC, for incident 200 GeV electrons. Right: the precision of the extrapolated DWC X position on the first HGCAL module as a function of incident electron energy assuming that the DWC resolution was Gaussian and can be modelled through a stochastic (σ_s) and constant term (σ_c).

surements were computed. The width of the residual distribution was considered to be the position resolution of a given sensor. Similar studies have already been performed for other highly-granular calorimeter prototypes, e.g. in [15] and [16].

5.3.1 Reference measurement

The reconstructed impact positions were compared to a straight line fit extrapolation from two delay wire chambers [17] (DWC) located 147 cm and 273 cm upstream of the first HGCAL module, which measure the trajectory of the incoming beam particle before it showers in the calorimeter prototype. The table supporting the HGCAL prototype at CERN had some vertical drift with time. In order to correct for these movements relative to the stationary DWCs, the coordinate systems were aligned for each run individually, applying the MILLEPEDE formalism [18]. After alignment we estimated the precision of the DWC by comparing the measurements from each chamber. We found a precision of between 570 μm (200 GeV particles) and 700 μm (20 GeV particles). An example of the DWC resolution is demonstrated in the left plot figure 29, which shows the difference in horizontal (X) coordinate recorded by the two DWC for 200 GeV electrons. The width of this distribution divided by $\sqrt{2}$ is about 570 μm, representing the intrinsic resolution of the DWC. Events were rejected from the analysis if the reconstructed coordinates in the DWCs differed by more than 1 mm with respect to their mean difference, to reduce the effects of noise in the DWC. The trajectories measured by the DWC were extrapolated to the HGCAL, where the precision of the position of incidence was estimated. Figure 29 (right) shows the precision of the extrapolation as a function of electron energy assuming Gaussian DWC resolution. The beam impact position on the HGCAL was thus known to a precision of a couple of mm.

5.3.2 Position reconstruction

Equation 5.5 defines the reconstructed shower impact position on a given layer:

$$\vec{x}_{\text{reco}} = \frac{\sum_i^{i\in M} \omega(E_i) \cdot \vec{x}_i}{\sum_i^{i\in M} \omega(E_i)}, \tag{5.5}$$

2018 JINST 13 P10023

where:

- The set M comprised either all cells on the investigated layer or cells within one(two) rings around the cell with maximum deposited energy (see section 3.5).
- $\omega(E_i)$ represents an energy weighting function.

Two degrees of freedom have been varied in order to both optimize the resolution and minimize the reconstruction bias towards preferred coordinates on the sensor (i.e. the centre of the cell and its edges — as would be the case in an unweighted barycentre estimator). It was found that a logarithmic weighting as in equation (5.6) using two rings around the cell with the maximum deposited energy (=19 cells) maximizes the precision for 250 GeV electron events in the first sensitive layer both for the X- and Y-coordinate, in data and simulation, while keeping any reconstruction bias towards sensor or cell centres at a minimum.

$$\omega(E_i) = \sum_{i}^{i \in M_{19}} \max\left(0.0,\ 3.5 + 1.0 \cdot \ln\left(\frac{E_i}{E_{\text{tot}}}\right)\right), \quad E_{\text{tot}} = \sum_{j}^{j \in M_{19}} E_j \tag{5.6}$$

Figure 30 shows the precision at the first sensitive layer, i.e. after six radiation lengths, as a function of the incident electron energy and compares those to simulation.[7] The figure includes the intrinsic resolution of the HGCAL layer as obtained from simulation in which the true electron impact position was well known. Comparison between data and simulation was performed on simulated samples that included the finite DWC resolution. The simulated DWC measurements were smeared according to their measured precision and event weights were used in the analysis to match the distribution of differences in horizontal and vertical positions as measured by the two DWC (see figure 29).

Figure 30 also summarizes the computed X-coordinate precision for all energies and layers as a function of their depth in the HGCAL stack. The precision improves with electron energy, as expected, reaching a constant value around 1.3 mm, somewhat higher than the intrinsic resolution (as seen by the simulation alone) of around 0.6 mm due to the resolution of the DWC. The solid horizontal line indicates the binary precision, i.e. the precision that would be obtained if the reconstruction maps an electron shower to the closest cell centre. Furthermore, the precision worsens with the depth in the calorimeter, which can be attributed to increased contributions from multiple scattering of low-energy secondary particles deeper into the shower.

The agreement between data and simulation including the DWC resolution smearing is within 10 % for most energies and layers. A fit of the form given by equation (5.7) quantifies the observed dependence w.r.t. the incident electron energy on the first layer.

$$\sigma_{x,y} = \frac{c_1}{\sqrt{E_e}} \oplus \frac{c_2}{E_e} \oplus c_3 \tag{5.7}$$

The individual contributions can be physically motivated[8] [19] and the fitted coefficients are listed in table 6.

[7] Data points for 100 GeV and 150 GeV were not available due to unsynchronised data streams between the DWC and HGCAL prototype.

[8] The $1/\sqrt{E}$ term is expected due to the stochastic nature of the energy deposits and the accuracy of these measurements varying as $1/\sqrt{E}$. The constant term arises from effects such as longitudinal shower development fluctuations. The 1/E term is related to the electronics noise etc.

2018 JINST 13 P10023

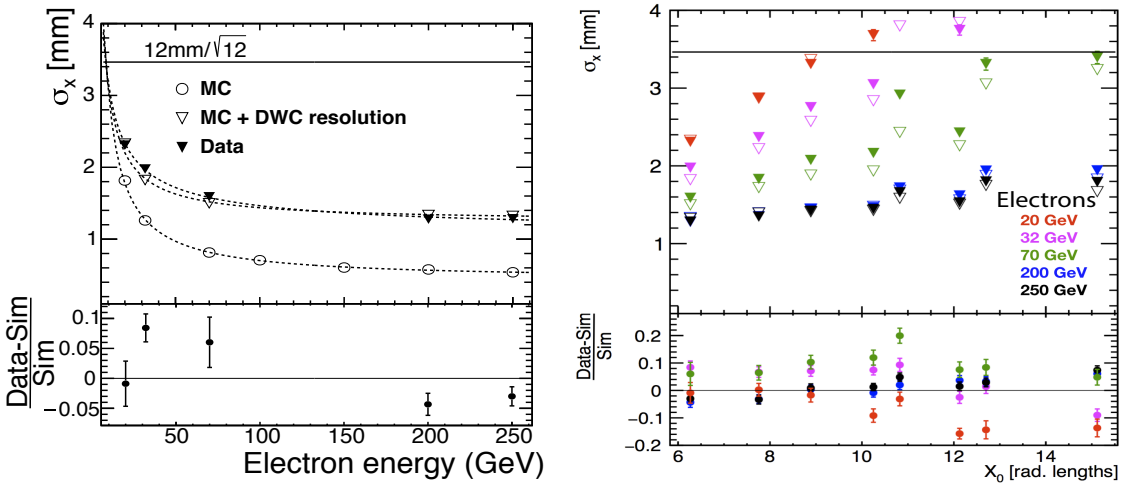

Figure 30. Left: residual widths of the X-coordinate reconstruction on the first sensitive layer as a function of incident electron energy. Right: the precision of the HGCAL sensors' X-coordinate measurement for all layers and for all energies. Both data and simulation (including the smearing by the DWC resolution) are shown. Open symbols are used for simulation; closed for data. Some points are off-scale.

Table 6. Spatial resolution contributions in the first sensitive sensor w.r.t. the electron energy.

Contribution	*x-coordinate*		*y-coordinate*	
	simulation	data	simulation	data
c_1 [$\sqrt{\text{GeV}}\cdot$ mm]	19.1 ± 0.8	10.9 ± 8.5	20.4 ± 0.7	18.5 ± 6.2
c_2 [GeV $\cdot$ mm]	5.6 ± 0.4	3.5 ± 2.2	1.6 ± 0.3	1.9 ± 1.7
c_3 [mm]	1.25 ± 0.01	1.0 ± 0.1	1.21 ± 0.01	1.04 ± 0.09

The intrinsic spatial precision of the HGCAL modules was better than 1 mm for electrons with energies above a few tens of GeV, i.e. for all electrons (and photons) of interest in the endcap regions of CMS. This is sufficient for matching calorimetric showers to tracks in the Tracker. Combining the measurements of all layers could lead to some additional improvement, not explored here.

6 Precision timing with silicon diodes and modules

An important consideration for all detectors for HL-LHC operation is their intrinsic evaluation of the timing of signals, due to the need to mitigate the effects of in-time event pileup. The HGCAL should be able to provide an estimation of the timing of electromagnetic and hadronic showers, with a precision of better than about 50 picoseconds. This information will be complementary to that provided by dedicated MIP timing detectors, planned to be placed in front of both the barrel and endcap calorimeters in CMS.

We have evaluated the intrinsic timing performance of single silicon diodes — unirradiated and irradiated, as well as complete prototype hexagonal sensors.

6.1 Precision timing with silicon diodes

In Spring 2016 sets of small silicon diodes [20] of two different types (p-on-n and n-on-p float-zone silicon) and thicknesses, previously irradiated to a range of neutron fluences representative of those

2018 JINST 13 P10023

expected in the HGCAL, were exposed to electron beams at CERN. The diodes measured 5×5 mm^2. The aim of this test was to compare the results on the intrinsic timing capabilities of the same diodes before irradiation [21] and after. The thicknesses of the diodes correspond approximately to those that will be used in the different regions of HGCAL: 120 μm sensors in the regions of highest fluence; 200 μm in the regions of intermediate fluence and 320 μm in the lowest fluence regions.

In order to prevent reverse annealing and to limit the leakage currents of the irradiated diodes, all diodes were operated in a cold box [22], operated at -30°C and flushed with dry nitrogen to prevent any humidity. After closing the box, achieving the required humidity and temperature took about 4–5 hours. To reduce the number of cooling cycles when switching sets of diodes, especially with tight constraints on beam time, all the diodes of a given type were hosted in the cold box at the same time, mounted in stacks on support plates, with 1 cm distance between each other, as shown in figure 31. Each stack comprised six diodes of the same type and thickness: two were unirradiated and acted as references; the remaining four were irradiated to different fluences. Table 7 summarizes the thicknesses and fluences of the diodes tested.

Table 7. Thicknesses and fluences of the irradiated diodes tested in 2016. Both n-on-p and p-on-n diodes were tested.

	Fluence (cm^{-2} 1 MeV neq)					
Thickness (μm)	Diode #1	Diode #2	Diode #3	Diode #4	Diode #5	Diode #6
120	0	0	6.25×10^{15}	6.25×10^{15}	1.00×10^{16}	1.60×10^{16}
200	0	0	1.50×10^{15}	2.50×10^{15}	2.50×10^{15}	4.00×10^{15}
320	0	0	4.00×10^{14}	6.00×10^{14}	6.00×10^{14}	9.00×10^{14}

The timing tests required large signals — tens or hundreds of MIPs — to be produced in the diodes from electromagnetic showers. Simulations showed that having a single absorber outside of the cold box resulted in large signals in the diodes closest to the absorber but those further away experienced far lower signals due to the transverse spread of the shower and small diode size. To increase the signals in the more downstream diodes, lead absorbers were placed inside the cold box upstream of each stack, as also shown in figure 31. The irradiated diodes were operated at both 600 and 800 V, while the non-irradiated ones at 600 V only. No difference in performance was found between the two irradiated-diode operating voltages. The waveforms from the diodes were digitized by a 5 GHz CAEN V1742 module, together with the trigger signal from the scintillator coincidence. Data were taken with electron beams of 100 and 150 GeV for p-type and n-type diodes, respectively.

The pulse amplitude and timing information were extracted from the digitized samples on an event-by-event basis, following the same procedure as in [21], as follows: the pedestal and noise were computed in an 8 ns-wide window prior to the rising edge of the signal. After pedestal subtraction a 20 ns time window was opened around the time of the trigger signal to search for the maximum amplitude. Since no external device for time reference was used (e.g. no MCP[9] or similar device), one of the diodes was used as a reference for the event reconstruction and time measurement. For each set of diodes, one unirradiated and one irradiated diode were used in turn as references: no significant difference was observed in terms of timing performance when using either reference. The noise for the unirradiated diodes was measured to be 10 ADC counts,

[9]Micro channel plates

2018 JINST 13 P10023

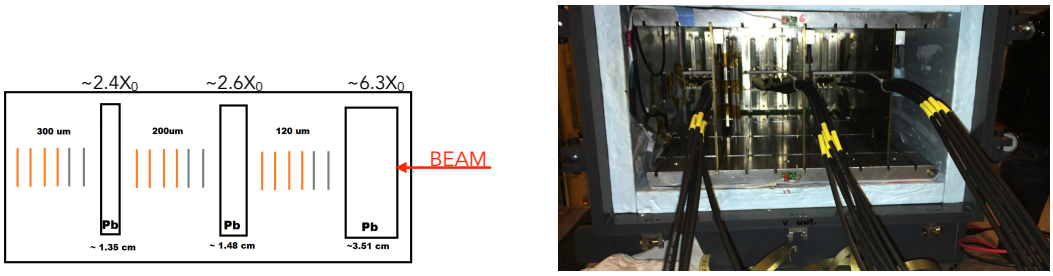

Figure 31. Left: layout of the 18 diodes hosted in the cold box. Three sets of diodes (120 µm, 200 µm, 320 µm) were placed downstream of Pb absorbers, of about 6.3, 2.6, 2.4 X_0 respectively. For each set, the 2 non-irradiated diodes (gray vertical lines) were followed by the irradiated ones (orange lines). Right: picture of the instrumented diodes placed in the cold box. The diodes were powered and readout via Cividec broadband amplifiers [23], placed outside the box and connected to the diodes, with cables passing through the box.

corresponding to about 1/3 of a MIP in the 200 µm diodes, in agreement with that found in 2014 for unirradiated diodes. The time was estimated with a constant fraction discrimination at 50% of the maximum amplitude.

As a first characterization of the sensor, the risetime, defined as the time for the pulse height to increase from 10% to 90% of its maximum amplitude, was measured for each diode. The results shown in figure 32 for p-on-n and n-on-p type diodes show that the signal response becomes faster both for thinner sensors and at higher fluences. This is because the irradiation process damages the depleted region with a resulting reduction of its effective thickness at a given voltage and correspondingly there was less distance for charges to traverse.

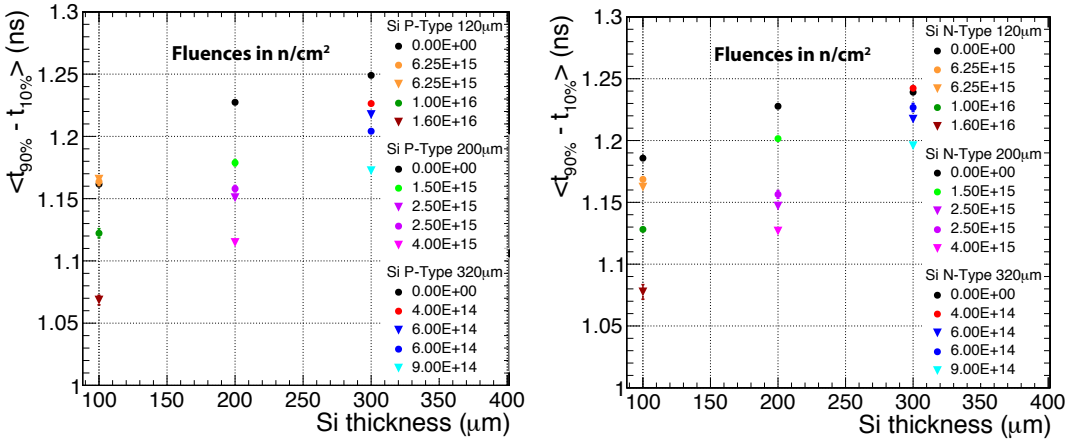

Figure 32. Pulse risetime, defined as the time taken for the pulse to increase from 10% to 90% of its maximum amplitude.

To estimate the timing capabilities of these devices, the timing measured by each diode was compared to that of an unirradiated diode of the same thickness and type. The obtained distributions were fitted with a Gaussian function in the range mean $\pm$ 2 $\times$ RMS. The timing resolution was then the Gaussian width, σ. Note that we required a minimum of 200 entries in the histograms to ensure good fits.

2018 JINST 13 P10023

In order to characterize the timing resolution as a function of the signal properties, we defined an effective signal-to-noise ratio $(S/N)_{\text{eff}}$, as in equation (6.1):

$$(S/N)_{\text{eff}} = \frac{(S/N)_{\text{ref}}(S/N)_n}{\sqrt{(S/N)^2_{\text{ref}} + (S/N)^2_n}} \tag{6.1}$$

where ref refers to the reference diode, compared against diode n.

For pairs of non-irradiated diodes, in order to estimate the timing resolution per device, the time difference can be divided by $\sqrt{2}$, in the hypothesis that the two measurements were independent and compatible. This procedure has been used to prove the compatibility of the time resolution for the unirradiated diodes measured in the 2016 test beam with the results obtained in 2014. For this comparison the same ADC-to-MIP calibration as measured in [21] was applied to the unirradiated diodes to estimate the timing performance as a function of the signal expressed in MIPs.

In figure 33, the resolution of the time difference is shown for the 320 µm thick diodes, as a function of the effective S/N.

The error bars on the Y axis account for statistical and systematic uncertainties, estimated by changing the range of each Gaussian fit to be the mean ± 3× RMS and mean ± 1.5 RMS, and also by reducing the minimum number of events for each distribution to 50. The trends corresponding to different radiation levels are shown with different colours and overlays as functions of $(S/N)_{\text{eff}}$. The plots show that the intrinsic timing resolution does not significantly depend on the fluence, at a given S/N ratio. The same observation can be made for the thinner silicon diodes, in spite of the lack of statistics.

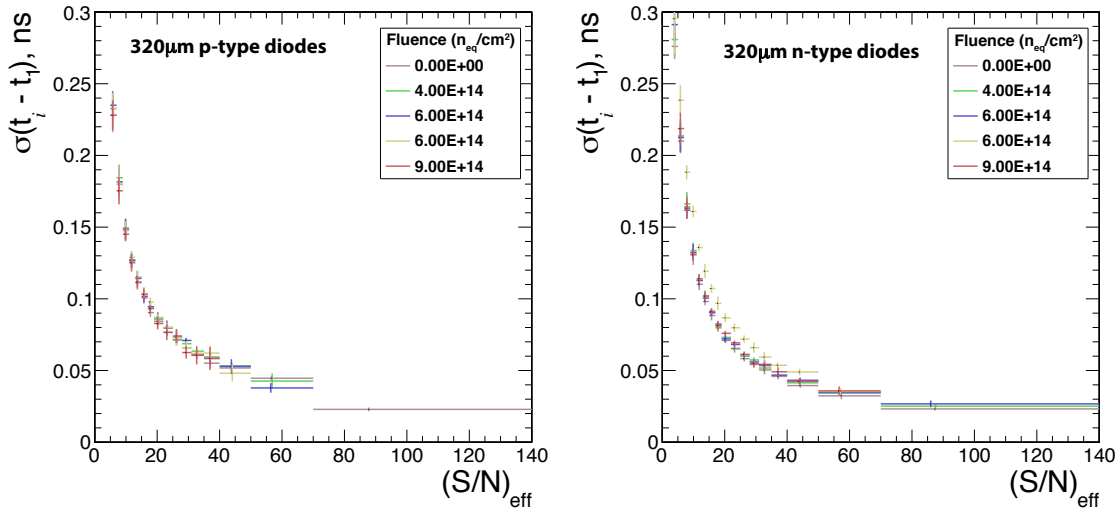

Figure 33. Resolution on the time difference between an unirradiated and an irradiated diode as a function of $(S/N)_{\text{eff}}$. Plots are shown for the 320 µm thick diodes of p-type (left) and n-type (right).

The timing performance can be directly compared between p- and n-type diodes, as in figure 34, where the timing resolution is shown for the 320 µm thick diodes for three different levels of radiation. These results indicate similar behaviours for both p- and n-type diodes as a function of S/N.

Table 8 shows the measured timing resolution on the single diodes, obtained by fitting the trends as a function of S/N with a three-parameter function as shown in equation (6.2) and quoting

2018 JINST 13 P10023

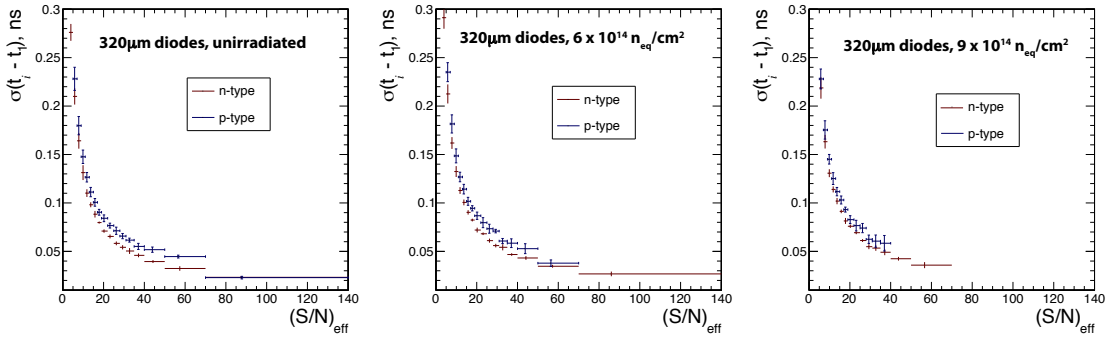

Figure 34. Resolution on the time difference between an unirradiated diode and one irradiated to a fluence level of 0 (left), 6.0×10^{14} (middle) and 9.0×10^{14} (right) neq/cm^2. In black for p-type and red for n-type.

the result at a value of S/N = 100. In this fit procedure, the C (constant) term was observed to vanish to zero for high values of the x axis, and the parameter A was not compatible with zero. A two parameter fit, as used in [21], was also tested but provided a worse description of the data points. The constant terms of the two-parameter fits are in any case reported in table 9. There are limitations in the amount of data available at the high energies (> 100 mips), which introduce significant errors to some points.

$$\sigma(t_{\text{ref}} - t_i) = \sqrt{\left(\frac{A}{\sqrt{(S/N)}}\right)^2 + \left(\frac{B}{S/N}\right)^2 + C^2} \tag{6.2}$$

Table 8. Resolution on the timing in units of ps for each silicon diode tested. The values reported in the table were extracted by evaluating the fit function in equation (6.2) at a value of S/N = 100, corresponding to about 30 MIPs.

	N-type			P-type		
Diode	120µm	200µm	320µm	120µm	200µm	320µm
2	11.7 ± 0.5	14.0 ± 3.0	16.5 ± 0.2	33.3 ± 1.9	18.2 ± 0.2	21.8 ± 0.5
3	15.1 ± 2.5	17.4 ± 2.5	18.1 ± 0.5	25.1 ± 6.9	19.1 ± 1.9	26.7 ± 2.6
4	16.7 ± 0.9	20.4 ± 2.3	19.1 ± 0.5	15.9 ± 5.9	15.8 ± 2.6	23.6 ± 1.4
5	20.6 ± 1.5	18.4 ± 2.3	22.3 ± 0.9	n/a	n/a	23.5 ± 1.1
6	n/a	19.4 ± 2.2	19.4 ± 3.9	n/a	n/a	22.0 ± 1.3

6.2 Precision timing with modules

As a next step in the program of characterizing precision timing measurements with the HGCAL detector we equipped a single 320 µm thick hexagonal sensor with dedicated fast readout electronics. Twenty five (from 135) central hexagonal cells were connected to their own amplifier chain, for a total gain of 100 per channel. The readout of the timing layer was performed using the same CAEN 5 GHz V1742 digitizer mentioned in section 6.1. Figure 35 shows the sensor layout used for these measurements, and the PCB used for fast readout. Each HGCAL cell was equipped with an amplifier placed very close to the wirebonded readout, and a 1:2 transformer to lower the input impedance to provide a faster rise time of the signals. An example waveform is also shown in

2018 JINST 13 P10023

Table 9. Resolution on the timing in units of ps for each silicon diode tested, extracted from the constant term of a two-parameter fit function as in [21].

	N-type			P-type		
Diode	120µm	200µm	320µm	120µm	200µm	320µm
2	10.8 ± 3.1	14.0 ± 3.0	16.3 ± 1.9	31.8 ± 5.6	17.7 ± 2.2	20.0 ± 2.1
3	10.8 ± 6.5	16.3 ± 4.4	18.9 ± 3.8	n/a	25.1 ± 6.1	38.1 ± 3.5
4	10.7 ± 6.3	19.9 ± 3.8	21.8 ± 3.4	n/a	n/a	32.5 ± 4.5
5	16.6 ± 4.6	19.2 ± 4.1	24.6 ± 4.9	n/a	n/a	38.6 ± 5.0
6	n/a	22.8 ± 4.2	26.1 ± 3.8	n/a	n/a	40.5 ± 6.3

figure 35. An additional amplifier was placed at the periphery of the PCB. The noise contributions from the electronics chain were measured to be less than 1 MIP equivalent in FNAL, and slightly worse at CERN due to the presence of additional attenuators (see below).

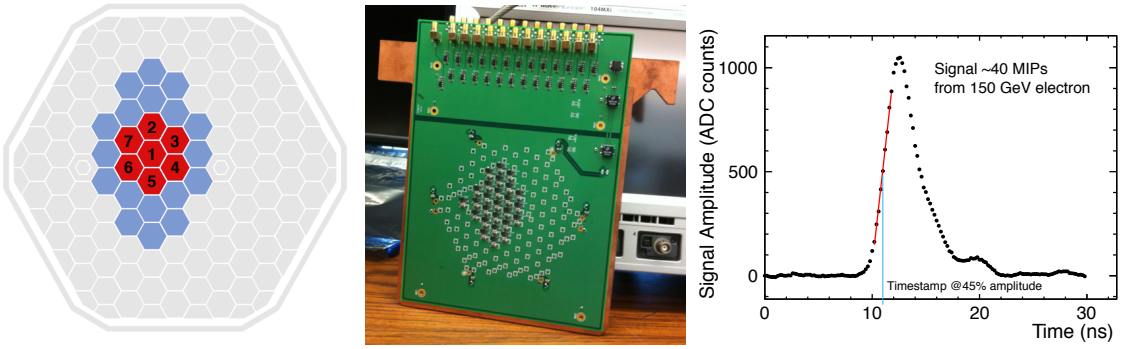

Figure 35. Left: the 25-cell section of the HGCAL silicon sensor that was read out in the timing measurements; Centre: the dedicated PCB designed for fast readout of the HGCAL sensor, which is wire-bonded to the PCB on its back side; Right: example waveform seen from the passage of a 150 GeV electron shower through the detector.

Measurements were performed in 2016 at FNAL and at CERN. At FNAL we used the primary 120 GeV proton beam and secondary mixed beams with energies ranging from 4 GeV to 32 GeV. Stacks of tungsten or lead plates with varying thicknesses were placed immediately upstream of the timing layer in order to measure the response along the longitudinal direction of the electromagnetic shower. A small plastic scintillator of transverse dimensions 1.8 mm×2 mm was used as a trigger counter to initiate the readout of the DAQ system and to select incident beam particles over a small geometric area, allowing us to centre the beam particles on the silicon sensor. Finally, a Photek 240 micro-channel plate photomultiplier (MCP-PMT) detector was placed further downstream to provide a very precise reference timestamp. The time resolution between a pair of Photek 240 detectors was previously measured to be 9.6 ps [24], hence the time resolution of a single Photek 240 was $9.6/\sqrt{2} = 6.8$ ps.

At CERN we used the SPS H2 line as for the single diode tests, exploiting the wider range of electron energies available — from 20 GeV to 250 GeV. To avoid saturation of the CAEN digitizer, 10 dB attenuators were placed between the output of the HGCAL sensor board and the digitizer input. For events impacting on the centre of a silicon pad we observed saturation of the onboard amplifiers for energies of 100 GeV and above. Events impinging at the edge of the sensor, when

2018 JINST 13 P10023

the shower activity spreads over multiple cells, did not produce any saturated signals. A stack of tungsten plates, separated from each other by about 7 mm, were used as absorbers. The silicon sensor was placed downstream of the last absorber layer, after an additional airgap of about 5 mm. The Photek 240 reference counter was placed about 1 m downstream of the sensor with an additional 8 X_0 of tungsten plates between them. A single low-noise 40 mm×40 mm scintillator counter was used as a trigger. The impact point on the silicon sensor was reconstructed with the DWC mentioned previously. The SPS H2 beams used had an RMS width of about 1.5 cm. This allowed the complete illumination of a single silicon cell of the HGCAL sensor as well as the ring of pads around it sufficently well to measure the timing resolution as a function of the impact point.

A linear fit to the pulses was performed from 20% to 90% of the signal amplitude. The timestamp was defined as the time at which the signal reaches 45% amplitude on this fit. The signal risetime was measured to be about 2 ns (defined as 10–90% of the amplitude, as for the single diodes), and was dominated by the electronic components.

We then measured the time difference between the HGCAL timing layer and the Photek MCP-PMT. Events were selected to pass identification criteria consistent with showering electrons by requiring a large deposit in the Photek MCP-PMT. This selection had high efficiency in discriminating shower events, since those produced many secondary particles that were then detected by the MCP-PMT positioned behind the absorber.

For the data from the FNAL test the information from seven cells (central cell plus 6 nearest neighbours) was combined to determine the overall timestamp of the HGCAL timing layer. Each cell used in the combination had to pass both charge and amplitude cuts (charge > 10 fC and amplitude > 0.01 V). The overall timing was calculated as a charge-weighted average of the seven cells. Due to the relatively low energy of the FNAL electron beams the average number of cells passing the cuts was 3–4.

An example time difference distribution is shown in figure 36 for 32 GeV electrons, where we measured about 16 psec resolution from the width of the distribution. As the alignment of the trigger counter restricted the data sample to events impinging on the centre of the central silicon cell the timing performance was very much dominated by the timing performance of the central cell.

A similar procedure was followed at CERN, except the threshold charge per cell was lowered from 10 fC to 6 fC. Deposits with > 110 pC were rejected since the amplifier saturated above this level. The precision of the Photek MCP was found to be around 20 ps, attributed to dispersion in arrival time of particles due to the large amount of material between the timing layer and the MCP. Consequently, we estimated the timing precision of the silicon by comparing two neighbouring cells in the timing layer.

The absolute time measured by each cell (+ amplifier chain) showed a significant amplitude dependence of up to 100 ps across the amplitude range explored. This is illustrated in figure 36 where we show the estimated time as a function of the input signal size. We accounted for this dependency with a parametric correction.

The timing performance measured at CERN was slightly worse than that measured at FNAL, which we attribute to the additional components in the readout chain.

The resolution of the time measured by two neighbouring cells, as a function of the effective S/N, is shown in figure 37, using incident electrons at energies between 100 and 250 GeV at CERN. A precision of better than 20 ps was achieved for $(S/N)_{\text{eff}}$ above about 100, compatible with the precision measured with single diodes.

2018 JINST 13 P10023

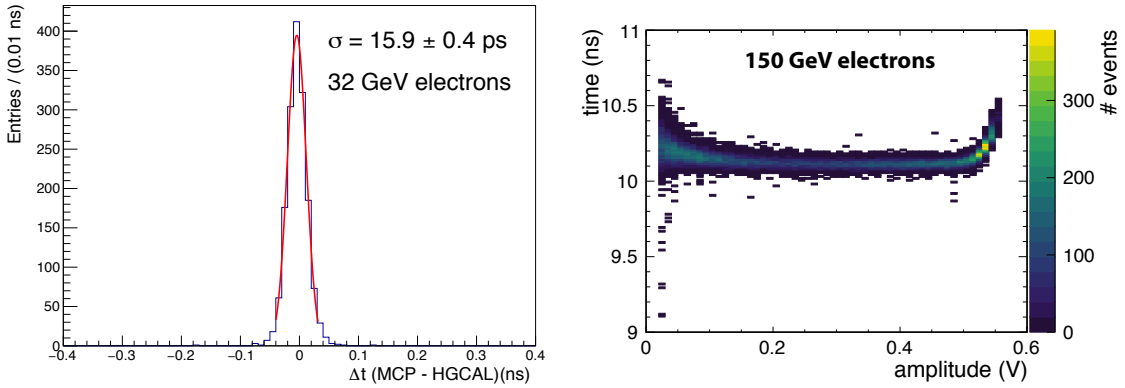

Figure 36. Left: time difference between the timestamps of the MCP-PMT and HGCAL timing layer for FNAL 32 GeV electrons, with $6X_0$ tungsten absorber 1 mm from the silicon. The beam impact point was contrainted by a trigger counter with 2 mm transverse size, aligned with the centre of the central cell. Information from all 7 cells was combined with charge weighting. Right: timewalk measured at CERN for the most energetic cell, which was subsequently corrected using a parametric fit.

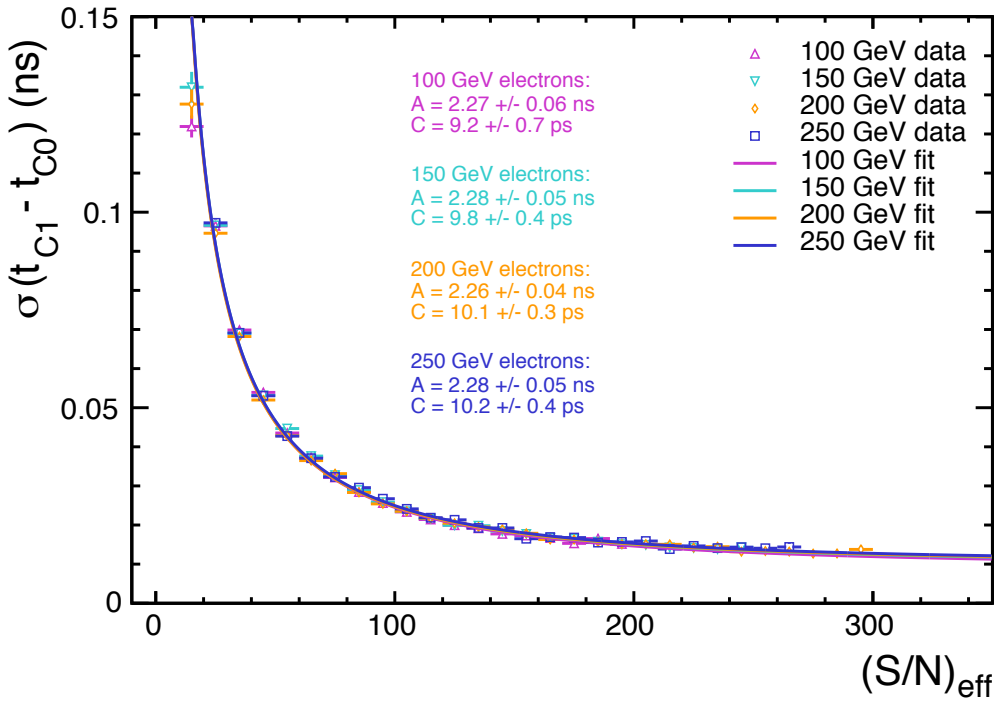

Figure 37. Resolution on the time difference between neighbouring hexagonal cells of a 6" 300 µm thick p-on-n hexagonal silicon sensor, as a function of $(S/N)_{\text{eff}}$.

7 Summary

The extensive series of tests performed on prototype diodes and modules have validated the concepts of the silicon section of the CMS High Granularity Calorimeter. Despite having a limited number of modules, the flexibility of the mechanical support structure has facilitated the testing of several

2018 JINST 13 P10023

configurations, focusing on different longitudinal parts of the electromagnetic shower. The measured basic quantities, such as shower shapes and energy distributions, match well with the GEANT4-based simulations, lending credence to the use of the simulation to fine-tune the design of the HGCAL. The intrinsic performance of the silicon-based calorimeter, in terms of energy resolution, spatial precision and timing, has been measured and also compares well with simulation. The measured energy resolution is limited by the relatively small number of layers, leading to a constant term of a few percent, not representative of the final HGCAL but matching well with simulation. A spatial precision of better than 1 mm can be achieved for electrons above a few tens of GeV, sufficient for matching calorimetric showers to tracks in the Tracker. The intrinsic timing performance is tens of picoseconds, again for reasonably high energy deposits, as will be the case for a majority of the layers in the HGCAL even for rather modest incoming particle energies.

References

[1] CMS collaboration, *The Phase-2 Upgrade of the CMS Endcap Calorimeter*, CERN-LHCC-2017-023 (2017).

[2] CMS collaboration, *Technical proposal for the Phase-II upgrade of the CMS detector*, CERN-LHCC-2015-010 (2015).

[3] S. Callier et al., *SKIROC2, front end chip designed to readout the Electromagnetic CALorimeter at the ILC*, 2011 *JINST* **6** C12040.

[4] *Fermilab Testbeam Facility*, http://ftbf.fnal.gov.

[5] *H2 beam line*, http://sba.web.cern.ch/sba/BeamsAndAreas/h2/H2manual.html.

[6] *CALICE collaboration*, https://twiki.cern.ch/twiki/bin/view/CALICE/CalicePapers.

[7] *Zedboard*, http://zedboard.com/product/zedboard.

[8] P. Rubinov, *Development of flexible, scalable, low cost readout for beam tests of High granularity calorimeter for the CMS endcap*, CMS-CR-2016-453 (2016).

[9] GEANT4 collaboration, S. Agostinelli et al., *GEANT4: A Simulation toolkit*, *Nucl. Instrum. Meth.* **A 506** (2003) 250.

[10] *CMSSW software for CMS*, https://twiki.cern.ch/twiki/bin/view/CMSPublic/WorkBookCMSSWFramework.

[11] *NA61/Shine experiment*, http://shine.web.cern.ch.

[12] B. Loo, F. Goulding and D. Gao, *Ballistic deficits in pulse shaping amplifiers*, *IEEE Trans. Nucl. Sci.* **35** (1988) 114.

[13] *GEANT4 reference physics lists*, http://geant4.cern.ch/support/proc_mod_catalog/physics_lists/referencePL.shtml.

[14] Particle Data Group collaboration, C. Patrignani et al., *Review of particle physics*, *Chin. Phys.* **C 40** (2016) 100001.

[15] D. Acosta et al., *Localizing particles showering in a spaghetti calorimeter*, *Nucl. Instrum. Meth.* **A 305** (1991) 55.

[16] V. Gorodnichev et al., *Study of position resolution and electron-hadron separation of electromagnetic calorimeter with a silicon structure*, *Nucl. Instrum. Meth.* **A 343** (1994) 47.

2018 JINST 13 P10023

[17] J. Spanggaard, *Delay wire chambers — A users guide*, SL-Note-98-023 (1998).

[18] V. Blobel, *Software alignment for tracking detectors*, *Nucl. Instrum. Meth.* **A 566** (2006) 5.

[19] R. Wigmans, *Calorimetry*, Clarendon Press, Oxford U.K. (2000).

[20] E. Currás et al., *Radiation hardness and precision timing study of silicon detectors for the cms High Granularity Calorimeter (HGC)*, *Nucl. Instrum. Meth.* **A 845** (2016) 60.

[21] N. Akchurin et al., *On the timing performance of thin planar silicon sensors*, *Nucl. Instrum. Meth.* **A 859** (2017) 31.

[22] T. Maenpaa et al., *Silicon beam telescope for LHC upgrade tests*, *Nucl. Instrum. Meth.* **A 593** (2008) 523.

[23] *C2 Broadband Amplifier, 2 GHz, 40 dB*, https://cividec.at/files/15_pdf.pdf.

[24] A. Ronzhin et al., *Study of the timing performance of micro-channel plate photomultiplier for use as an active layer in a shower maximum detector*, *Nucl. Instrum. Meth.* **A 795** (2015) 288.

2018 JINST 13 P10023